

# Dynamical properties of AMAZE and LSD galaxies from gas kinematics and the Tully-Fisher relation at $z \sim 3$ <sup>★</sup>

A. Gnerucci<sup>1</sup>, A. Marconi<sup>1</sup>, G. Cresci<sup>2</sup>, R. Maiolino<sup>3</sup>, F. Mannucci<sup>2</sup>, F. Calura<sup>4</sup>, A. Cimatti<sup>6</sup>, F. Cocchia<sup>3</sup>,  
A. Grazian<sup>3</sup>, F. Matteucci<sup>5</sup>, T. Nagao<sup>7</sup>, L. Pozzetti<sup>8</sup>, and P. Troncoso<sup>3</sup>

<sup>1</sup> Dipartimento di Fisica e Astronomia, Università degli Studi di Firenze, Largo E. Fermi 2, 50125 Firenze, Italy  
e-mail: gnerucci@arcetri.astro.it

<sup>2</sup> INAF-Osservatorio Astrofisico di Arcetri, Largo E. Fermi 5, 50125 Firenze, Italy  
e-mail: [gcresci; filippo]@arcetri.astro.it

<sup>3</sup> INAF-Osservatorio Astronomico di Roma, via di Frascati 33, Monte Porzio Catone, Italy  
e-mail: maiolino@oa-roma.inaf.it

<sup>4</sup> Jeremiah Horrocks Institute for Astrophysics and Supercomputing, University of Central Lancashire, Preston PR1 2HE, UK

<sup>5</sup> Dipartimento di Astronomia, Università di Trieste, via Tiepolo 11, 34131 Trieste, Italy

<sup>6</sup> Dipartimento di Astronomia, Università di Bologna, via Ranzani 1, 40127 Bologna, Italy

<sup>7</sup> Research Center for Space and Cosmic Evolution, Ehime University, 2-5 Bunkyo-cho, Matsuyama 790-8577, Japan

<sup>8</sup> INAF-Osservatorio Astronomico di Bologna, via Ranzani 1, 40127 Bologna, Italy

Received 23 July 2010 / Accepted 22 December 2010

## ABSTRACT

We present a SINFONI integral-field kinematical study of 33 galaxies at  $z \sim 3$  from the AMAZE and LSD projects, which are aimed at studying metallicity and dynamics of high-redshift galaxies. The number of galaxies analyzed in this paper constitutes a significant improvement over existing data in the literature, and this is the first time that a dynamical analysis is obtained for a relatively large sample of galaxies at  $z \sim 3$ . Eleven galaxies show ordered rotational motions ( $\sim 30\%$  of the sample). In these cases we estimate dynamical masses by modeling the gas kinematics with rotating disks and exponential mass distributions. We find dynamical masses in the range  $2 \times 10^9 M_{\odot} - 2 \times 10^{11} M_{\odot}$  with a mean value of  $\sim 2 \times 10^{10} M_{\odot}$ . By comparing observed gas velocity dispersion with what is expected from models, we find that most rotating objects are dynamically “hot”, with intrinsic velocity dispersions of  $\sim 90 \text{ km s}^{-1}$ . The median value of the ratio between the maximum disk rotational velocity and the intrinsic velocity dispersion for the rotating objects is 1.6, much lower than observed in local galaxies value ( $\sim 10$ ) and slightly lower than the  $z \sim 2$  value (2–4). Finally we use the maximum rotational velocity from our modeling to build a baryonic Tully-Fisher relation at  $z \sim 3$ . Our measurements indicate that  $z \sim 3$  galaxies have lower stellar masses (by a factor of ten on average) compared to local galaxies with the same dynamical mass. However, the large observed scatter suggests that the Tully-Fisher relation is not yet “in place” at these early cosmic ages, possibly owing to the young age of galaxies. A smaller dispersion of the Tully-Fisher relation is obtained by taking the velocity dispersion into account with the use of the  $S_{0.5}$  indicator, suggesting that turbulent motions might play an important dynamical role.

**Key words.** galaxies: evolution – galaxies: formation – galaxies: fundamental parameters – galaxies: high-redshift – galaxies: kinematics and dynamics

## 1. Introduction

The dynamical properties of galaxies play a fundamental role in the context of galaxy formation and evolution. The observed dynamics of galaxies represent a test to theoretical models and are the most direct way to probe the content of dark matter. In particular, the dynamical mass of a galaxy inferred from its rotation curve is the most direct way to constrain mass and angular momentum of dark matter halos, which can be compared with the predictions of cosmological cold dark matter models of hierarchical structure formation. In such models (Blumenthal et al. 1984; Davis et al. 1985; Springel et al. 2006; Mo et al. 1998) mergers are believed to play an important role for galaxy

formation and evolution. However, the observational evidence for the existence of rotating disks with high star formation rates at  $z \sim 2$  suggests that smooth accretion of pristine gas is also an important mechanism that drives star formation and mass assembly at high redshift (Epinat et al. 2009; Wright et al. 2009; Förster Schreiber et al. 2009; Cresci et al. 2009).

In recent years, our observational knowledge in this field has increased enormously. Many dynamical studies have been performed on extended samples of  $z \sim 1-2.5$  objects (Genzel et al. 2006, 2008; Förster Schreiber et al. 2006, 2009; Cresci et al. 2009; Erb et al. 2006; Law et al. 2007, 2009; Epinat et al. 2009; Wright et al. 2007, 2009). However, little is known on the dynamics of galaxies at  $z \gtrsim 2.5$ , where only a few particular objects have been investigated (Nesvadba et al. 2006, 2007, 2008; Jones et al. 2010; Law et al. 2009; Lemoine-Busserolle et al. 2010; Swinbank et al. 2007, 2009).

The redshift range  $z \sim 3-4$  is particularly important to study since it occurs before the peak in the cosmic star formation rate (see, for example, Dickinson et al. 2003; Rudnick et al. 2006;

<sup>★</sup> Based on observations collected with European Southern Observatory/Very Large Telescope (ESO/VLT) (proposals 075.A-0300, 076.A-0711 and 178.B-0838), with the Italian TNG, operated by FGG (INAF) at the Spanish Observatorio del Roque de los Muchachos, and with the *Spitzer Space Telescope*, operated by JPL (Caltech) under a contract with NASA.

**Table 1.** Galaxy properties and observation setups.

Object	Sample	RA <sup>1</sup>	Dec <sup>1</sup>	$z/\text{scale}(\text{kpc}''\text{)}^2$	$T_{\text{exp}}(\text{min})$	Pixel scale (")	Line used <sup>3</sup>
SSA22a-M38	AMAZE	22:17:17.7	+00:19:00.7	3.294/7.48	400	0.125 × 0.25	[OIII]
SSA22a-C16	AMAZE	22:17:32.0	+00:13:16.1	3.068/7.65	350	0.125 × 0.25	[OIII]
CDFS-2528	AMAZE	03:32:45.5	-27:53:33.3	3.688/7.18	350	0.125 × 0.25	[OIII]
SSA22a-D17	AMAZE	22:17:18.9	+00:18:16.8	3.087/7.64	250	0.125 × 0.25	[OIII]
CDFA-C9	AMAZE	00:53:13.7	+12:32:11.1	3.212/7.54	250	0.125 × 0.25	[OIII]
CDFS-9313	AMAZE	03:32:17.2	-27:47:54.4	3.654/7.21	250	0.125 × 0.25	[OIII]
CDFS-9340 <sup>(4)</sup>	AMAZE	03:32:17.2	-27:47:53.4	3.658/7.20	250	0.125 × 0.25	[OIII]
CDFS-11991	AMAZE	03:32:42.4	-27:45:51.6	3.661/7.25	450	0.125 × 0.25	[OIII]
3C324-C3	AMAZE	15:49:47.1	+21:27:05.0	3.289/7.49	150	0.125 × 0.25	[OIII]
DFS2237b-D29	AMAZE	22:39:32.7	+11:55:51.7	3.370/7.43	250	0.125 × 0.25	[OIII]
CDFS-5161	AMAZE	03:32:22.6	-27:51:18.0	3.660/7.20	300	0.125 × 0.25	[OIII]
DFS2237b-C21	AMAZE	22:39:29.0	+11:50:58.0	3.403/7.40	200	0.125 × 0.25	[OIII]
SSA22a-aug96M16	AMAZE	22:17:30.9	+00:13:10.7	3.292/7.48	250	0.125 × 0.25	[OIII]
Q1422-D88	AMAZE	14:24:37.9	+23:00:22.3	3.752/7.13	250	0.125 × 0.25	[OIII]
CDFS-6664	AMAZE	03:32:33.3	-27:50:7.4	3.797/7.11	500	0.125 × 0.25	[OIII]
SSA22a-C36	AMAZE	22:17:46.1	+00:16:43.0	3.063/7.65	100	0.125 × 0.25	[OIII]
CDFS-4414	AMAZE	03:32:23.2	-27:51:57.9	3.471/7.34	350	0.125 × 0.25	[OIII]
CDFS-4417 <sup>(4)</sup>	AMAZE	03:32:23.3	-27:51:56.8	3.473/7.34	350	0.125 × 0.25	[OIII]
CDFS-12631	AMAZE	03:32:18.1	-27:45:19.0	3.709/7.17	250	0.125 × 0.25	[OIII]
CDFS-13497	AMAZE	03:32:36.3	-27:44:34.6	3.413/7.39	150	0.125 × 0.25	[OIII]
CDFS-14411	AMAZE	03:32:20.9	-27:43:46.3	3.599/7.25	200	0.125 × 0.25	[OIII]
CDFS-16272	AMAZE	03:32:17.1	-27:42:17.8	3.619/7.24	350	0.125 × 0.25	[OIII]
CDFS-16767	AMAZE	03:32:35.9	-27:41:49.9	3.624/7.24	300	0.125 × 0.25	[OIII]
Cosmic eye <sup>5</sup>	AMAZE	21:35:12.7	-01:01:42.9	3.075/ <sup>5</sup>	200	0.125 × 0.25	[OIII]
Abell1689-1 <sup>5</sup>	AMAZE	13:11:30.0	-01:19:15.3	3.770/ <sup>5</sup>	300	0.125 × 0.25	[OIII]
Abell1689-2 <sup>5</sup>	AMAZE	13:11:25.5	-01:20:51.9	4.868/ <sup>5</sup>	400	0.125 × 0.25	[OII]
Abell1689-4 <sup>5</sup>	AMAZE	13:11:26.5	-01:19:56.8	3.038/ <sup>5</sup>	240	0.125 × 0.25	[OIII]
SSA22b-C5	LSD	22:17:47.1	+00:04:25.7	3.117/7.61	240	0.05 × 0.1 (AO)	[OIII]
SSA22a-C6	LSD	22:17:40.9	+00:11:26.0	3.097/7.63	280	0.125 × 0.25 (AO)	[OIII]
SSA22a-M4 <sup>4</sup>	LSD	22:17:40.9	+00:11:27.9	3.098/7.63	280	0.125 × 0.25 (AO)	[OIII]
SSA22a-C30	LSD	22:17:19.3	+00:15:44.7	3.104/7.62	240	0.05 × 0.1 (AO)	[OIII]
Q0302-C131	LSD	03:04:35.0	-00:11:18.3	3.240/7.51	240	0.05 × 0.1 (AO)	[OIII]
Q0302-C171	LSD	03:04:44.3	-00:08:23.2	3.34/7.44	240	0.05 × 0.1 (AO)	[OIII]
DSF2237b-D28	LSD	22:39:20.2	+11:55:11.3	2.938/7.75	240	0.05 × 0.1 (AO)	[OIII]
Q0302-M80	LSD	03:04:45.7	-00:13:40.6	3.416/7.39	240	0.05 × 0.1 (AO)	[OIII]
DSF2237b-MD19	LSD	22:39:21.1	+11:48:27.7	2.616/7.99	200	0.05 × 0.1 (AO)	H $\alpha$

**Notes.** <sup>(1)</sup> J2000. <sup>(2)</sup> Redshifts are measured from the observed [OIII] line wavelength. <sup>(3)</sup> [OIII] denotes the [OIII] $\lambda\lambda$  5007, 4959 Å doublet; H $\alpha$  the H $\alpha$   $\lambda$  6563 Å line. <sup>(4)</sup> The object is in the same field of view of the object on the previous line. <sup>(5)</sup> Lensed objects not analyzed in this paper. The spatial scale (pc'') depends on the lensing model.

Hopkins & Beacom 2006; Mannucci et al. 2007), when only a small fraction ( $\sim 15\%$ , Pozzetti et al. 2007) of the stellar mass in present-day galaxies has been assembled. It is also the redshift range where the most massive early-type galaxies are expected to form (see, for example, Saracco et al. 2003). Moreover, the number of galaxy mergers is much greater than at later times (Conselice et al. 2007; Stewart et al. 2008). As a consequence, the predictions of different models tend to diverge significantly at  $z \gtrsim 2.5$ .

This paper is based on two projects focused on studying the metallicity and dynamics of high-redshift galaxies: AMAZE (Assessing the Mass-Abundance redshift Evolution) (Maiolino et al. 2008a,b) and LSD (Lyman-break galaxies Stellar populations and Dynamics) (Mannucci & Maiolino 2008; Mannucci et al. 2009). Both projects use integral-field spectroscopy of samples of  $z \sim 3$ –4 galaxies in order to derive their chemical and dynamical properties. In both projects we make use of data obtained with the Spectrograph for Integral Field Observations in the Near Infrared (SINFONI) at the Very Large Telescope (VLT) of the European Southern Observatory (ESO). Integral field spectroscopy has proven to be a powerful tool to study galaxy dynamics as it provides two dimensional velocity maps,

without the restrictions of longslit studies, also plagued by unavoidable light losses.

The AMAZE sample consists of  $\sim 30$  Lyman Break Galaxies in the redshift range  $3 < z < 4.8$  (most of which at  $z \sim 3.3$ ), with deep Spitzer/IRAC photometry (3.6–8  $\mu\text{m}$ ), an important piece of information to derive reliable stellar masses. These galaxies were observed with SINFONI in seeing-limited mode. The LSD sample is a representative, albeit small, sample of 10 LBGs at  $z \sim 3$  with available Spitzer and HST imaging from the Steidel et al. (2003) catalogue. For LSD SINFONI observations were performed with the aid of adaptive optics in order to improve spatial resolution since this project was aimed to obtain spatially-resolved spectra for measuring kinematics and gradients in emission lines. The global sample is listed in Table 1.

Lyman Break Galaxies are objects selected based on the Ly-break technique and based on their UV rest-frame blue color. As a consequence these samples are biased both against dust reddened systems and against aged stellar populations, which are characterized by redder colors. Therefore, the conclusions inferred from our results apply only to a sub-population (about half) of galaxies at  $z \sim 3$  (Reddy et al. 2005; van Dokkum et al. 2006; Grazian et al. 2007).

In this paper we focus on the dynamics of AMAZE and LSD galaxies at  $z \sim 3$ . In Sect. 2 we present observations, data reduction and the method followed to extract kinematical maps from integral-field spectra. In Sect. 3 we present the results and a simple method to individuate the objects with a velocity map consistent with a rotating disk. In Sect. 4 we describe the “rotating disk” model adopted in this paper, explain our “fitting strategy” to constrain model parameters and estimate their errors. In Sect. 4.3 we discuss the results of model fitting on the selected subsample of objects consistent with rotating disks. In Sect. 5 we discuss fit results and present the Tully-Fisher relation at  $z \sim 3$  (Sect. 5.2).

In the following, we adopt a  $\Lambda$ CDM cosmology with  $H_0 = 70 \text{ km s}^{-1} \text{ Mpc}^{-1}$ ,  $\Omega_m = 0.3$  and  $\Omega_\Lambda = 0.7$ .

## 2. Observations and data reduction

Complete descriptions of the AMAZE and LSD programs, of their observations and data reduction are presented in Maiolino et al. (2008a) and Mannucci et al. (2009). Here we report a brief summary on observations and data reduction.

The near-IR spectroscopic observations were obtained by means of SINFONI, the integral-field spectrometer at VLT (Eisenhauer et al. 2003). For AMAZE galaxies, SINFONI was used in its seeing-limited mode, with the  $0.125'' \times 0.25''$  pixel scale and the H+K grism, yielding a spectral resolution  $R \sim 1500$  over the spectral range  $1.45\text{--}2.41 \mu\text{m}$ . For the LSD galaxies, SINFONI was used with the Adaptive Optics module using a bright star close to the galaxy to guide the wavefront correction system. The pixel scale used is of  $0.05'' \times 0.10''$  (for all objects except SSA22a-C6 and SSA22a-M4 for which was used the  $0.125'' \times 0.25''$  pixel scale). The (*K*-band) seeing during the observations was generally about  $0.6''\text{--}0.7''$ . In the AO assisted observations the spatial resolution obtained is  $\sim 0.2''$ .

Data were reduced by using the ESO-SINFONI pipeline (version 3.6.1). The pipeline subtracts the sky from the temporally contiguous frames, flat-fields the images, spectrally calibrates each individual slice and then reconstructs the cube. Individual cubes were aligned in the spatial direction using the offsets of the position of the [OIII] or H $\alpha$  line emission peak. Within the pipeline the pixels are resampled to a symmetric angular size of  $0.125'' \times 0.125''$  or  $0.05'' \times 0.05''$ . The atmospheric absorption and instrumental response were taken into account and corrected by dividing with a suitable standard star.

In Table 1 we summarize all the relevant properties and observation setups of the objects presented in this paper.

In the AMAZE sample there is a subsample of 4 lensed objects. We decided not to analyze these objects in this paper because of the uncertainties introduced by the lensing model and the associated de-projection. They will be discussed in a forthcoming paper.

### 2.1. Extraction of the gas kinematics

We extract the kinematics of the gas by fitting the emission line spectrum for each spatial pixel of the cube corresponding to a given position on the sky. In order to improve the signal-to-noise ratio (hereafter  $S/N$ ) we first perform a smoothing of the cube spatial planes, by using a Gaussian filter with  $FWHM$  of 3 pixels. This is smaller than the spatial resolution of the observations which usually corresponds to a Point Spread Function with a  $FWHM$  of at least 4 pixels.

In all cases, but one, we fit the profile and shift of [OIII] $\lambda\lambda 5007, 4959 \text{ \AA}$  doublet. The two [OIII] lines are parametrized using single Gaussian functions with the following, physically motivated constraints: the two lines are forced to have the same average velocity  $v$  and velocity dispersion  $\sigma$ , while their flux ratio is fixed,  $F_{4959}/F_{5007} = 0.33$ , since both the lines are emitted from the same upper energy level of the O $^{2+}$  ion. For one object at  $z \sim 2.6$  we fit the H $\alpha$  line with a single Gaussian function. Since we perform the fit of the spectrum within a spectral window of only  $\sim 0.2 \mu\text{m}$  around the line, the continuum level is simply set to the mean continuum flux in this band.

To automatically exclude noise fluctuations or bad pixels and to take into account the effect of instrumental broadening we constrain the velocity dispersion of the lines to be higher than the instrumental resolution estimated from the sky emission lines. We define the signal-to-noise ratio ( $S/N$ ) of each line as the peak of the line model divided by the rms of the spectrum estimated in regions with no emission lines. Finally, we reject all fits where the  $S/N$  is lower than 2.

Uncertainties on measured fluxes, velocities and velocity dispersions are obtained from the formal errors on best fit parameters. Such errors are computed after two iterations of the line fitting procedure: in the second fit we adopt pixel by pixel errors equal to the rms of the residuals in the first fit.

## 3. Results

In Figs. 1 to 6 we present the kinematical maps for all the objects described in Table 1. This paper is dedicated only to the study of galaxy dynamical properties while other studies (e.g. integrated properties, metallicity, etc.) have been or will be presented in other dedicated papers (Maiolino et al. 2008a; Mannucci et al. 2009, 2010; Cresci et al. 2010; and Troncoso et al. 2010, in prep.).

In the majority of the AMAZE sample (17 out of 23 objects, i.e.  $\sim 72\%$ , excluding the four lensed objects) the morphology of line flux maps is simple, characterized by single peak distributions with typical dimensions of  $\sim 1\text{--}1.5''$  and relatively low ellipticities of the isophotes. These morphologies are likely the consequence of beam smearing since the typical seeing in this data is  $\sim 0.6\text{--}0.7''$   $FWHM$  (see below for a more accurate estimation). However, in some cases we find a secondary clump or asymmetric extended emission (e.g. in SSA22-M38).

In the galaxies from the LSD sample we find more complex morphologies which are likely the consequence of the AO-assisted observations providing higher spatial resolution ( $\sim 0.2''$   $FWHM$ ) which allows us to spatially resolve more complex structures, but lower sensitivity to extended sources given the higher surface brightness detection threshold.

There are three cases of close pairs of objects with similar brightnesses. CDFS-9313 and CDFS-9340 have a projected plane of the sky separation of  $\sim 1.0''$  ( $\sim 7$  kpc at the average redshift of the sources); CDFS-9340 is redshifted by  $\sim 280 \text{ km s}^{-1}$  with respect to CDFS-9313, the brightest of the pair. CDFS-4414 and CDFS-4417 have a projected separation of  $\sim 1.2''$  ( $\sim 9$  kpc); CDFS-4414 is blueshifted by  $\sim 120 \text{ km s}^{-1}$  with respect to the brighter companion. SSA22a-C6 and SSA22a-M4, from the LSD sample, have a projected separation of  $\sim 1.6''$  ( $\sim 12$  kpc) and SSA22a-M4 is redshifted by  $\sim 90 \text{ km s}^{-1}$  with respect to the brighter companion.

Inspection of the velocity maps in Figs. 1 to 6 reveals a number of objects with a clear and regular velocity gradient (12 out of 22 objects in the AMAZE sample and only one out of 9 in

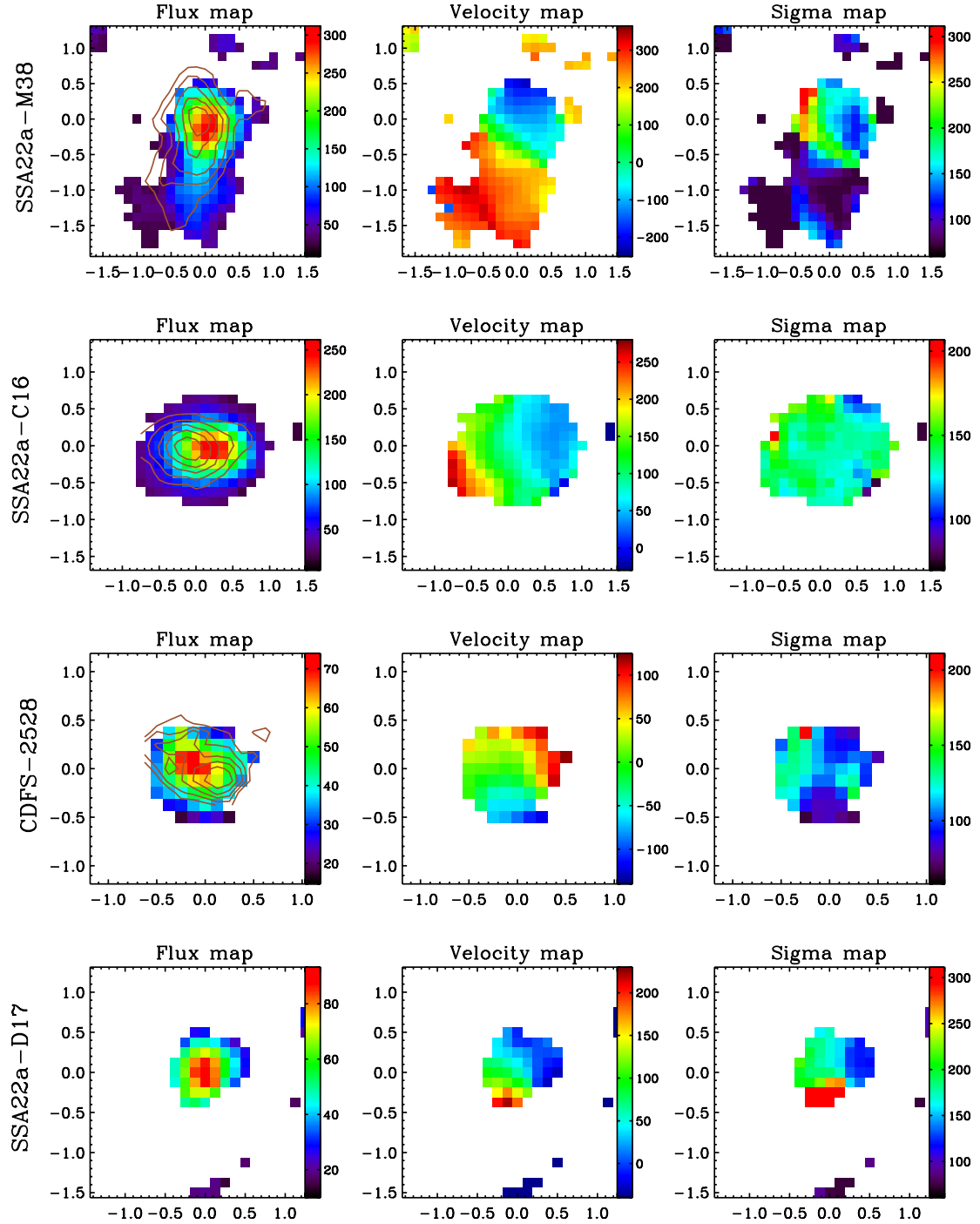


**Fig. 1.** Kinematical maps for objects *SSA22A-M38*, *SSA22A-C16*, *CDFS-2528* and *SSA22A-D17* (from the top respectively). Respectively, from the left: flux, velocity and sigma map. the  $X - Y$  coordinates are in arcseconds referred to an arbitrary object center position. The north direction is the positive  $Y$  axis. The vertical color bars are in arbitrary units for the flux map and in  $\text{km s}^{-1}$  for the velocity and sigma maps. Overplotted on the flux map the continuum flux distribution (brown isophotes) for the object whenever we detect a continuum flux component with sufficient  $S/N$ .

the LSD sample). The presence of such velocity gradients is an indication of possible rotating-disk kinematics. The identification of rotating objects and their distinction from complex kinematics cases or mergers is important for the comparison with theoretical models. Some authors (Förster Schreiber et al. 2009; Cresci et al. 2009) used the technique developed by Shapiro et al. (2008) based on kinemetry (Krajnović et al. 2006) to quantify asymmetries in both the velocity and sigma maps in order to empirically differentiate between rotating and non rotating systems.

This technique is not useful when applied to the data presented in this paper due to the low  $S/N$  that does not allow us to recover with sufficient accuracy the needed kinemetry parameters. We assess the presence of such velocity gradients by using a different approach. We fit the velocity map with a plane (i.e.  $v = ax + by + v_0$ ) and classify the object as “rotating” or “not rotating” if the velocity map is well fitted (or not) by a plane. In detail we use the  $\chi^2$  statistic to accept or reject the hypothesis that the velocity map is well fitted by a plane: we accept the

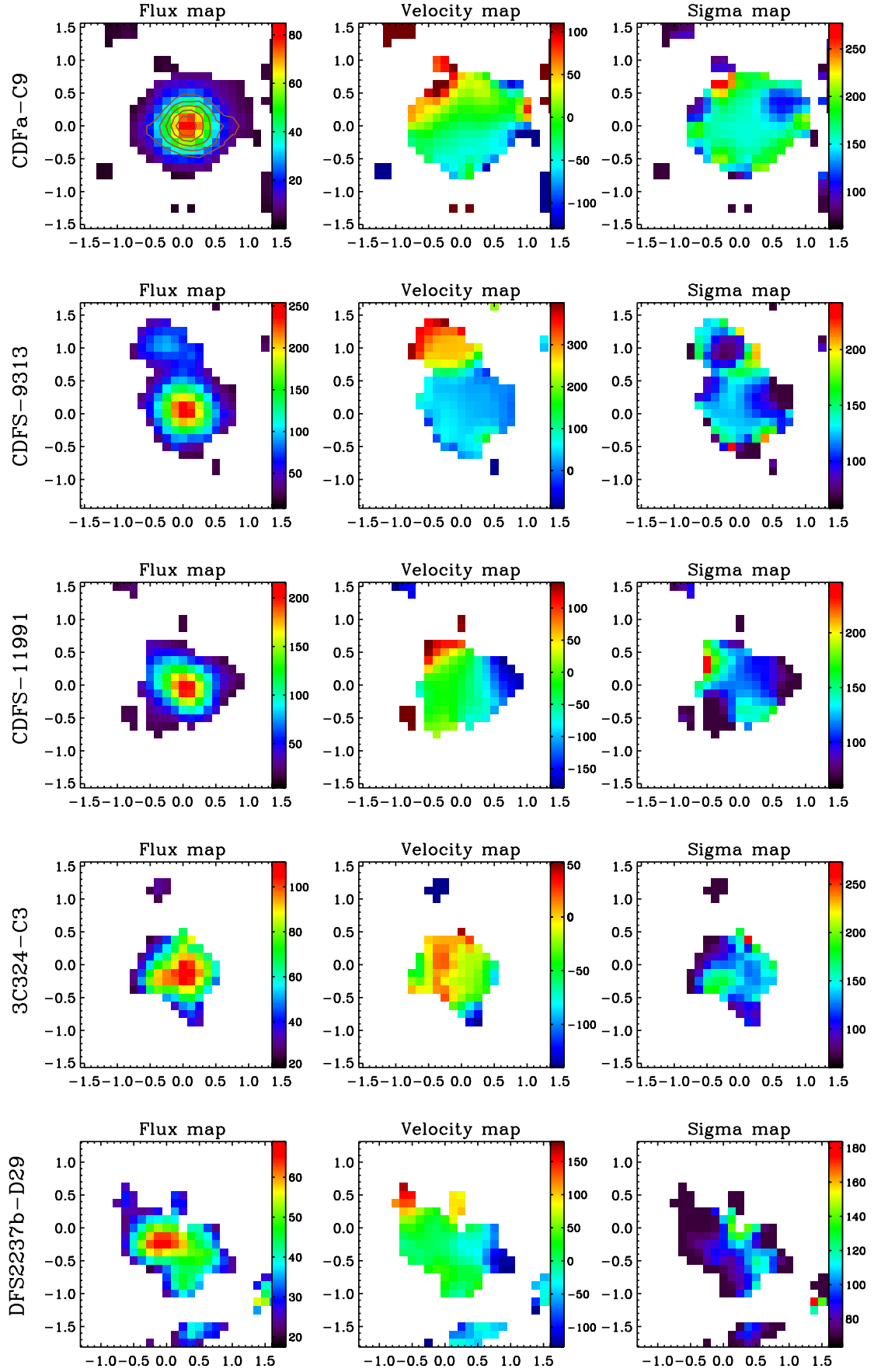


**Fig. 2.** Kinematic maps for the objects (respectively from the top) CDFa-C9, CDFS-9313 (in the same field of view the fainter source at the north-west is CDFS-9340), CDFS-11991, 3C324-C3 and DFS2237b-D29. Panels, axis and color bar indications same as in Fig. 1.

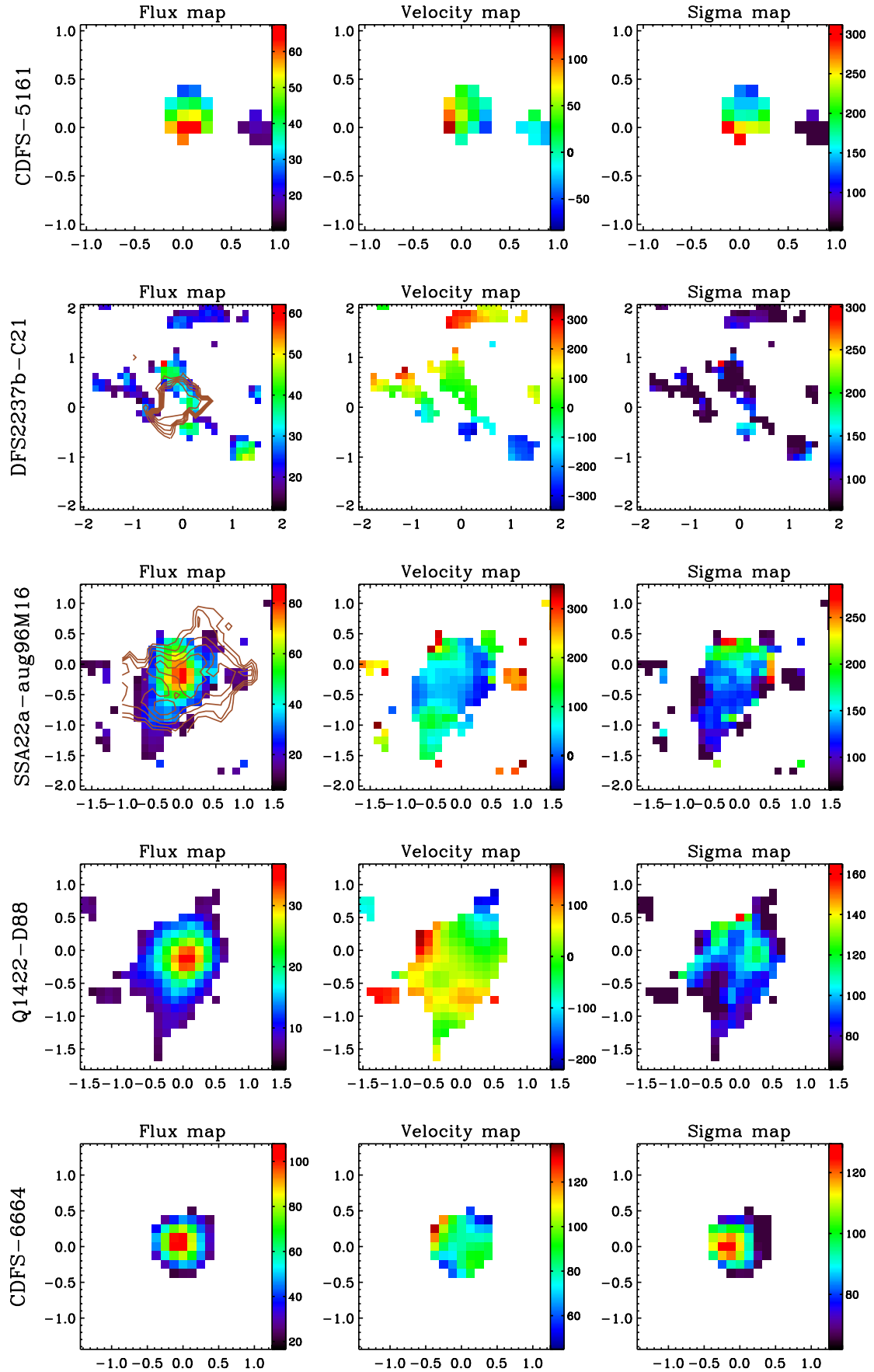


**Fig. 3.** Kinematic maps for the objects (respectively from the top) *CDFS-5161*, *DFS2237b-C21*, *SSA22a-aug96M16*, *Q1422-D88* and *CDFS-6664*. Panels, axis and color bar indications same as in Fig. 1.

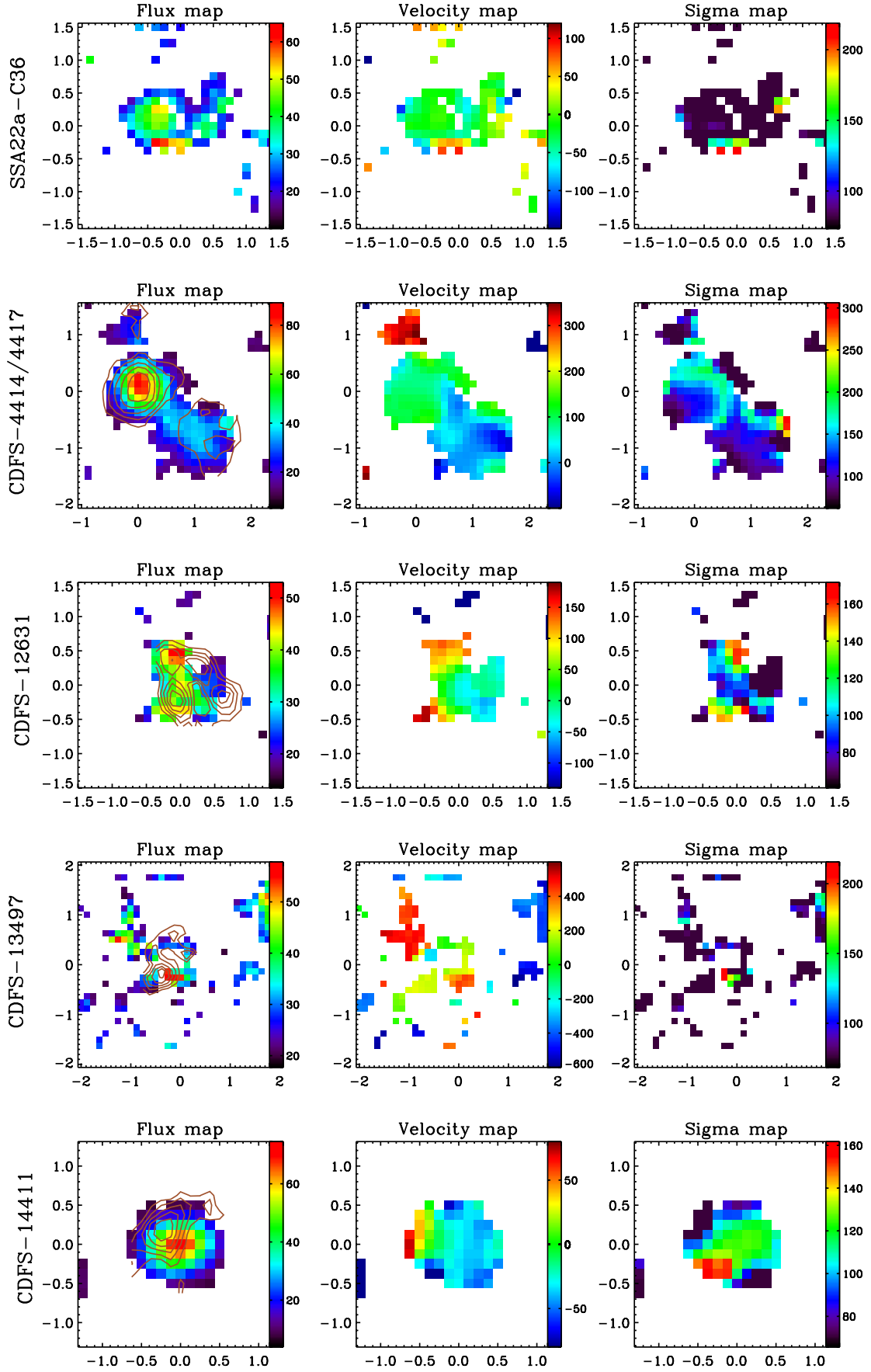


**Fig. 4.** Kinematic maps for the objects (respectively from the top) SSA22A-C36, CDFS-4414/4417 (CDFS-4417 is the brighter object at the north), CDFS-12631, CDFS-13497 and CDFS-14411. Panels, axis and color bar indications same as in Fig. 1.

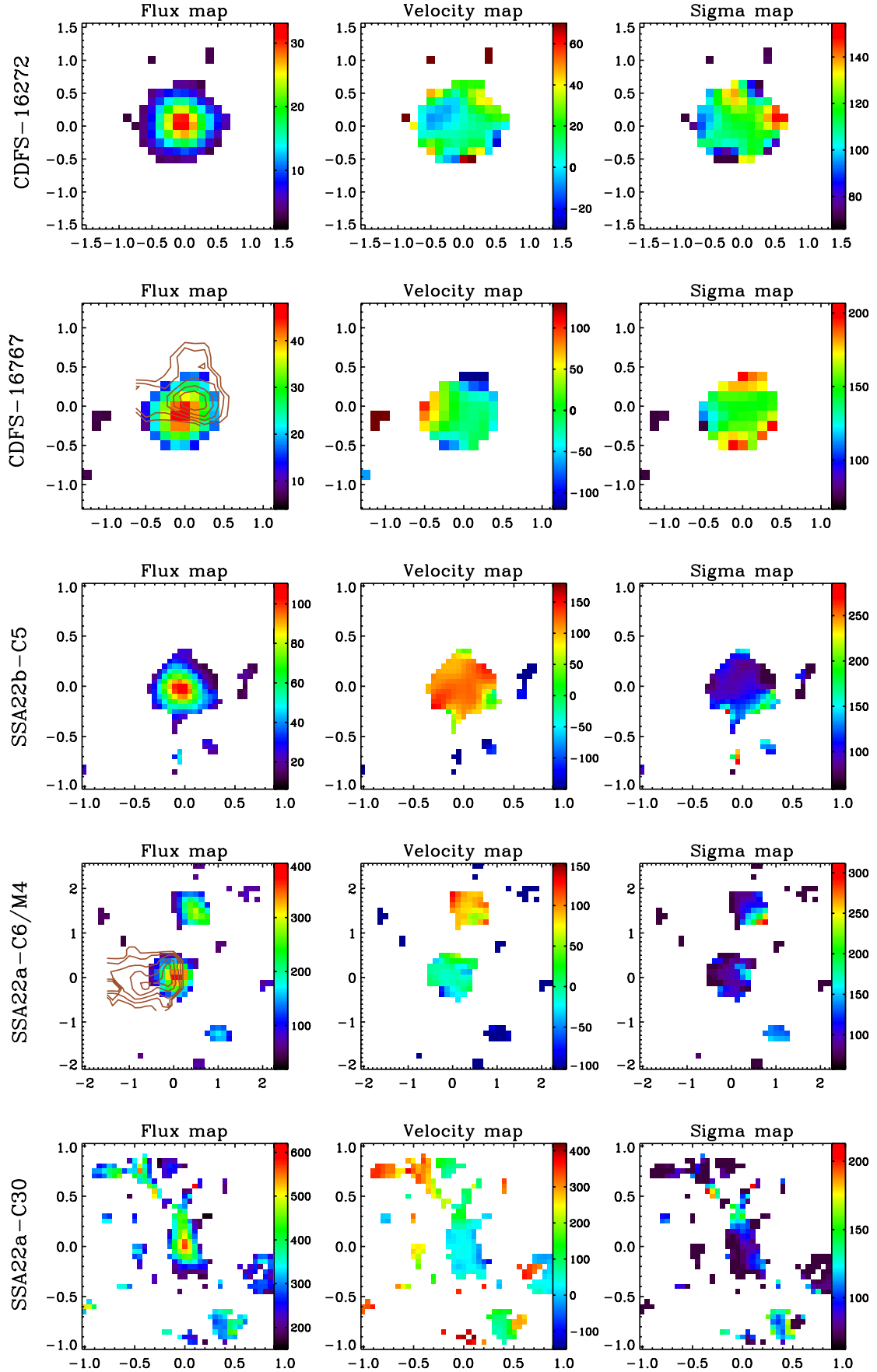


**Fig. 5.** Kinematic maps for the objects (respectively from the top) *CDFS-16272*, *CDFS-16767*, *SSA22b-C5*, *SSA22a-C6/M4* (*SSA22a-M4* is the fainter northern object) and *SSA22a-C30*. Panels, axis and color bar indications same as in Fig. 1.

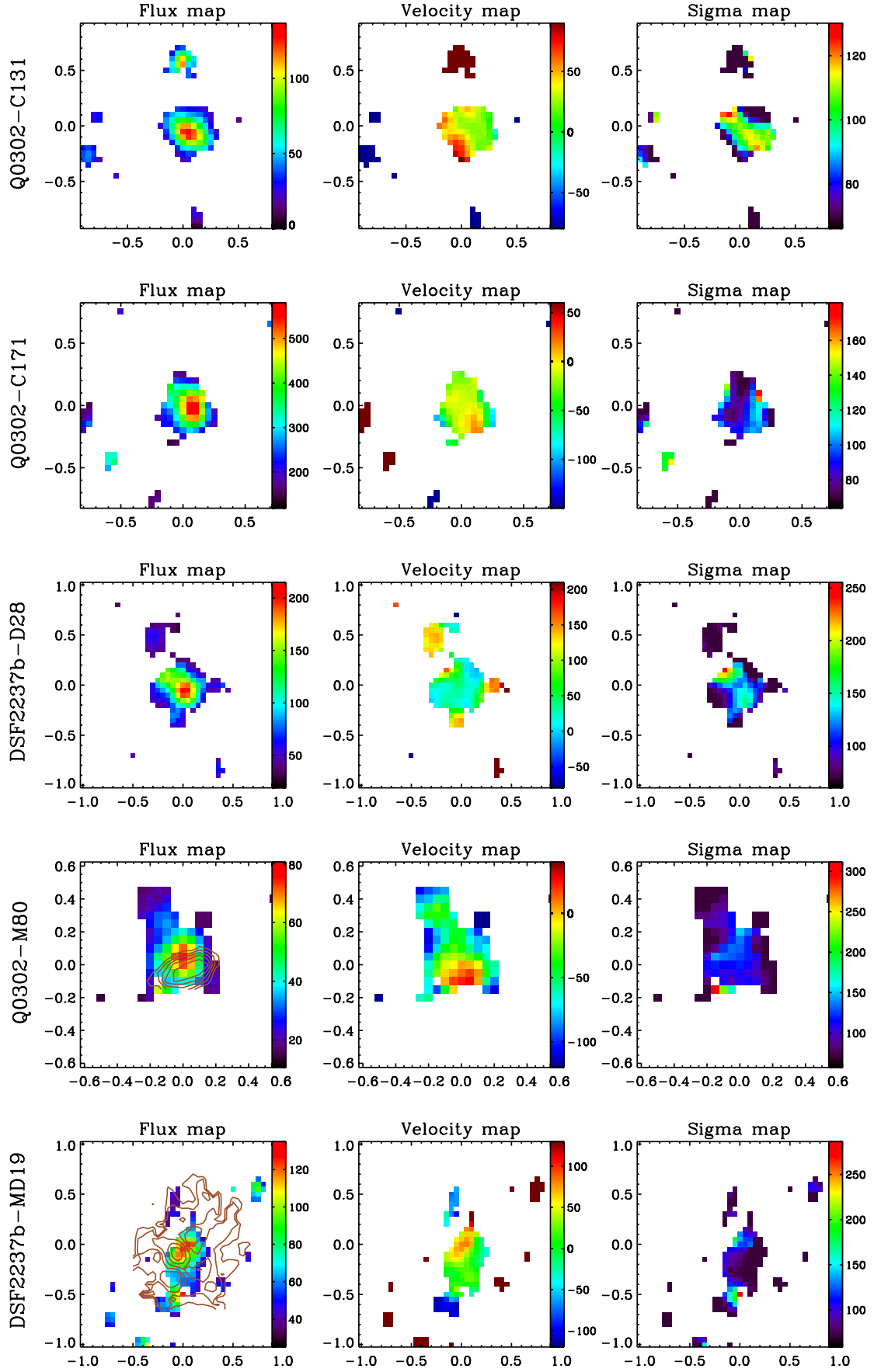


**Fig. 6.** Kinematic maps for the objects (*respectively from the top*) Q0302-C131, Q0302-C171, DSF2237b-D28, Q0302-M80 and DSF2237b-MD19. Panels, axis and color bar indications same as in Fig. 1.

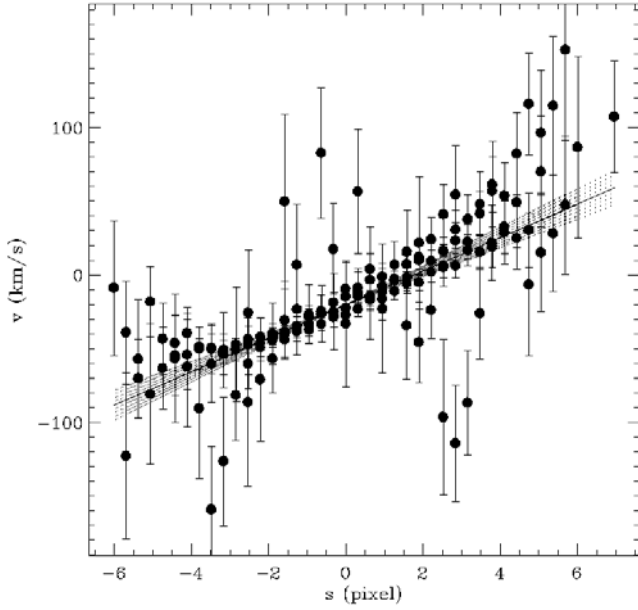


**Fig. 7.** Example of the method (applied to object *CDF A-C9*) for assessing the presence of a smooth gradient in the velocity map. The solid line shows the fitted plane seen from the edge, while the filled points show the observed velocity map on the projection. The dashed lines represent the 1, 2, 3, and  $4\sigma$  on the plane inclination.

hypothesis if there is a probability lower than the 4.6% (adopting a  $\chi^2$  distribution with the correct number of degree of freedom) to obtain a  $\chi^2$  value greater than the value obtained.

For objects with velocity maps well fitted by a plane we calculate its inclination relative to the  $X - Y$  plane (i.e. the magnitude of the velocity gradient). We confirm their “rotating” classification only if this inclination is inconsistent with zero at least a significance level of  $4\sigma$ . On the other hand a plane inclination consistent with zero might correspond either to genuinely non rotating object or to a rotating one seen face-on. In this case we cannot identify it as a rotating disk. In conclusion we classify the observed galaxies with the following criteria.

- if the velocity map shows a non zero gradient from plane fitting, we classify the object as “rotating”;
- if the velocity map is well fitted by a plane but its inclination is consistent with zero within  $4\sigma$ , we label the object as “not classifiable”;
- if the velocity map cannot be fitted with a plane, we classify the object as “not rotating”.

We choose to fit a “plane” to the velocity gradient because, due to the limited  $S/N$ , we are sampling mainly the linear part of the rotation curve of our targets. By using a plane we can adopt a simple model with only 3 free parameters and therefore we can rely on simpler statistics.

In principle we could have used also velocity dispersion maps to classify galaxies as “rotating” or “non rotating”: in fact, a circularly symmetric dispersion map is the expected signature of spatially unresolved rotation at the center of a rotating disk. However, we decided not to use them principally because we would have missed galaxies with regular rotation patterns in velocity, but whose velocity dispersion maps are distorted by turbulent and/or non-gravitational motions, as verified “a posteriori” with our modeling.

In Fig. 7 we show an example of our method. We plot the projection of the velocity map along the direction ( $s$ ) of

**Table 2.** Objects observed.

AMAZE Objects	$\chi^2/\text{d.o.f.}$	Classification
SSA22a-M38	3057/176	Rotating
SSA22a-C16	182/136	Rotating
CDFS-2528	61.6/52	Rotating
SSA22a-D17	20.6/42	Rotating
CDF A-C9	157/142	Rotating
CDFS-9313	63.8/91	Rotating
CDFS-9340	42.5/29	Rotating
CDFS-11991	226/99	Not rot.
3C324-C3	45.3/76	Rotating
DFS2237b-D29	229/107	Not rot.
CDFS-5161	2.00/12	Not clas.
DFS2237b-C21	725/141	Not rot.
SSA22a-aug96M16	680/119	Not rot.
Q1422-D88	478/127	Not rot.
CDFS-6664	15.9/40	Not clas.
SSA22a-C36	102/86	Not clas.
CDFS-4414	259/91	Not rot.
CDFS-4417	117/94	Not clas.
CDFS-12631	135/70	Not rot.
CDFS-13497	3133/91	Not rot.
CDFS-14411	62.7/68	Rotating
CDFS-16272	48.4/82	Not clas.
CDFS-16767	63.0/46	Rotating
LSD Objects		
SSA22b-C5	216/138	Not rot.
SSA22a-C6	101/54	Not rot.
SSA22a-M4	21.8/36	Not clas.
SSA22a-C30	19334/243	Not rot.
Q0302-C131	62.2/95	Rotating
Q0302-C171	170/102	Not clas.
DSF2237b-D28	1848/203	Not rot.
Q0302-M80	206/87	Not rot.
DSF2237b-MD19	268/95	Not rot.

maximum inclination of the fitted plane (i.e. the fitted plane seen from its edge). We also show the 1, 2, 3, and  $4\sigma$  slopes of the plane inclination.

The classification for all the objects is reported in Table 2.

Note that the object *SSA22a-M38* is classified as “rotating” even if its velocity map is not fitted by a plane (see the  $\chi^2$  value in Table 2). In this case the smooth velocity gradient is very clear and the  $S/N$  is high; the fit with a simple plane fails because of the flattening of the velocity field at the “red” and “blue” edges.

The next step is to model the gas kinematics of “rotating” galaxies to relate observed kinematics with the mass distribution.

## 4. Kinematical modeling

### 4.1. The model

The adopted dynamical model assumes that the ionized gas is circularly rotating in a thin disk. We neglect all hydrodynamical effects, therefore the disk motion is entirely determined by the gravitational potential.

In principle turbulent motions, often observed in high  $z$  rotating disk galaxies as well as in our own data, could provide significant dynamical support. Indeed [Epinat et al. \(2009\)](#) apply an asymmetric drift correction assuming that turbulent motions support mass. However, while stellar chaotic motions always support mass because they have gravitational origin, this is not always true for gas motions. The gas velocity dispersion might be strongly increased because of non gravitational motions (like,

e.g., in winds driven by starburst activity), and in that case it would not be directly linked to the dynamical mass. Therefore we adopted a conservative approach and neglected the contribution of the gas velocity dispersion. In any case we will, at most, underestimate the dynamical mass by a factor lower than  $\sim 2$  at the disk scale length (Epinat et al. 2009).

The galaxy gravitational potential is generated by an exponential disk mass distribution with surface density given by:

$$\Sigma(r) = \Sigma_0 e^{-r/r_e}. \quad (1)$$

The rotation curve of a thin disk with such mass distribution is (Binney & Tremaine 1987):

$$V_c(r)^2 = 4\pi G \Sigma_0 r_e y^2 [I_0(y)K_0(y) - I_1(y)K_1(y)] \quad (2)$$

where  $y = r/2r_e$  and  $I_n$ ,  $K_n$  are the modified Bessel functions of the first and second kind.

By defining the ‘‘dynamical mass’’ of the galaxy as the total mass enclosed in a 10 kpc radius (e.g. Cresci et al. 2009), we can finally write

$$V_c(r) = 6.56 \text{ km s}^{-1} \left( \frac{M_{\text{dyn}}}{10^{10} M_\odot} \right)^{0.5} \left( \frac{r}{\text{kpc}} \right) A(y) \quad (3)$$

where

$$A(y) = \left[ \frac{I_0(y)K_0(y) - I_1(y)K_1(y)}{I_0(y_{10})K_0(y_{10}) - I_1(y_{10})K_1(y_{10})} \right]^{0.5} \quad (4)$$

and  $y_{10}$  corresponds to  $y$  computed for  $r = 10$  kpc.

The velocity along the line of sight for a given position on the sky is derived from  $V_c(r)$  by taking into account geometrical projection effects.

Another important element of the model is the intrinsic flux distribution (hereafter IFD) of the emission line, since it acts as a weighting function in the calculation of the observed velocities and velocity dispersions when taking into account instrumental effects. Following Cresci et al. (2009) the IFD in the disk plane is modeled with an exponential function,

$$I(r) = I_0 e^{-r/r_0} \quad (5)$$

where  $r$  is the distance from the disk center and  $r_0$  is the scale radius. Such IFD is then projected onto the plane of the sky. Several objects in our sample have surface brightness distributions clearly different from those of exponential disks. However, given the low  $S/N$  and poor spatial resolution of our data, we decided to keep the IFD modeling as simple as possible (see also Cresci et al. 2009).

In computing the observed velocity shift and velocity dispersion we take into account the instrumental beam smearing. The spatial PSF is modeled with a two-dimensional Gaussian function with full width half maximum  $FWHM_{\text{PSF}}$ , sampled over the detector  $x$ ,  $y$  pixels. The instrumental spectral response is also described by a Gaussian function with sigma  $\sigma_{\text{inst}}$ . Finally, we calculate the model values for the three observed quantities:  $F_{\text{model}}(x_i, y_j)$ ,  $v_{\text{model}}(x_i, y_j)$  and  $\sigma_{\text{model}}(x_i, y_j)$  where  $x_i, y_j$  represent a spatial pixel in the data cube. For a detailed description of the model refer to Appendix B of Marconi et al. (2003).

Summarizing, the model parameters are:

- $x_c, y_c$ : coordinates in the plane of the sky of the disk dynamical center;
- $\theta$ : position angle (PA) of the disk line of nodes;
- $i$ : inclination of the disk;
- $M_{\text{dyn}}$ : dynamical mass;
- $r_e$ : characteristic radius of the exponential disk;
- $V_{\text{sys}}$ : systemic velocity of the galaxy.

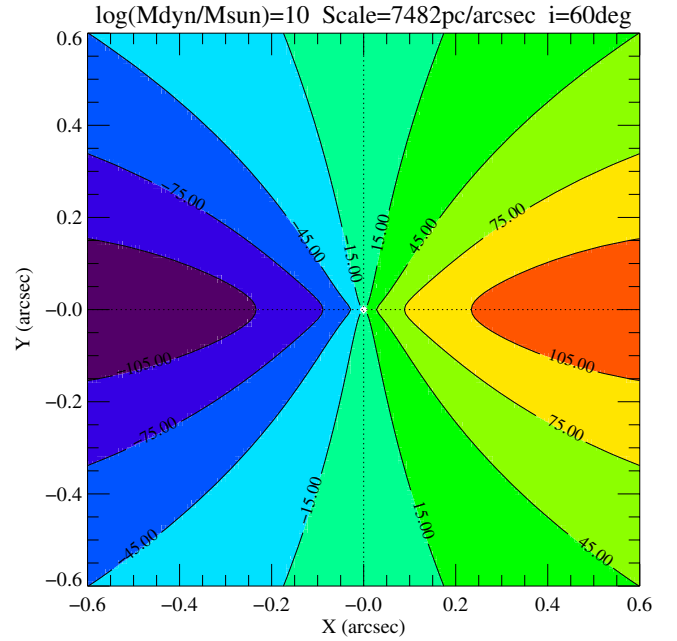


**Fig. 8.** Velocity field on the sky plane (‘‘spider diagram’’) for a simulated rotating disk at redshift  $z \sim 3.3$  with mass of  $10^{10} M_\odot$ , an exponential mass profile with characteristic radius of  $\sim 2.2$  kpc, inclination of  $60^\circ$  and velocities binned in steps of  $30 \text{ km s}^{-1}$ .

By using these parameters values we derive  $V_{\text{max}}$  that is the maximum velocity of the rotation curve. We will use this parameter in Sect. 5.2 to build the Tully-Fisher relation for our data sample.

## 4.2. Fit strategy

### 4.2.1. Preliminary steps

The first preliminary step of the model fitting is to estimate the spectral and spatial resolution of the observations, characterized by the corresponding  $\sigma_{\text{spec}}$  and  $FWHM_{\text{PSF}}$  of the Gaussian broadening functions.

The spectral resolution ( $\sigma_{\text{spec}}$ ) is simply estimated by using the profile of isolated lines in sky spectra.

Estimating the spatial resolution ( $FWHM_{\text{PSF}}$ ) is more complex since we miss datacubes of stars obtained with the same instrumental setting at the same time and at a similar position on the sky as the object datacube. We have therefore devised a method to estimate  $FWHM_{\text{PSF}}$  directly from the datacubes of the objects showing rotating-disk kinematics.

In the assumption that the kinematics is approximated by a rotating disk we expect an intrinsic line of sight velocity field on the sky plane as shown in Fig. 8, which illustrates the iso-velocity contours projected on the sky of a simulated galaxy with mass  $10^{10} M_\odot$  (the so called ‘‘spider diagram’’). The gas with line of sight velocity in a given velocity bin lies in the locus delimited by two subsequent iso-velocity contours. We can observe that the spatial extent of such region is always lower along the line of nodes direction (the  $X$ -axis) than in the perpendicular direction, and the central velocity bins show the minimal extent. For this reason we expect that an image of the object in the central velocity bins will be spatially unresolved along the line of nodes direction (see the example of Fig. 8: the central velocity bin of  $30 \text{ km s}^{-1}$  has an extent along the line of nodes direction

lower than  $\sim 0.1''$ , well below the typical value of our spatial resolution of  $\sim 0.6'' FWHM$ .

In practice, we select the spatial planes of the object datacube with wavelength close the line centroid, and for each of these spatial planes we fit the line surface brightness with a two dimensional Gaussian function. According to what is stated above, we take the minimum  $FWHM$  value from these two dimensional Gaussians as an estimate of  $FWHM_{PSF}$ .

We could test our method with one object, *CDFa-C9*, for which there is a star in the SINFONI field of view. The  $FWHM$  of this star is consistent within  $\sim 0.1''$  with our estimate of the spatial resolution. We also verified that our estimates are in good agreement with the  $FWHM$  of the telluric standard stars observed after the science exposures, although with different airmasses. Moreover, in the following, we will test how systematic errors on  $FWHM_{PSF}$  can affect the best fit model parameters.

The second preliminary step is the determination of the intrinsic flux distribution (IFD) to be used in the computation of the velocity maps. The exponential IFD in the disk plane is projected onto the plane of the sky, convolved by the PSF, averaged over the detector binsize and matched to the observed flux map by minimizing the following  $\chi^2$

$$\chi_{\text{flux}}^2 = \left[ \sum_{i,j} \frac{F(x_i, y_j) - F_{\text{model}}(x_i, y_j)}{\Delta F(x_i, y_j)} \right]^2 \quad (6)$$

the free parameters in this fit are the center position of the IDF in the plane of the sky ( $x_c, y_c$ ), the scale radius  $r_0$  and the position angle and inclination of the elliptical isophotes ( $I_0$ , the flux scale, is only a normalization factor).

From the fit of the IFD we also estimate some parameters needed in the model. As explained in the following section, we set the disk center position equal to the IFD center position ( $x_c, y_c$ ) and the mass distribution scale radius  $r_e$  equal to the IFD scale radius  $r_0$ . The inclination and position angle of the disk are instead determined from the fit of the velocity maps, but we use the estimates from the IFD fit as first guesses.

#### 4.2.2. Fitting of velocity maps

To estimate the free model parameters we minimize the following  $\chi^2$ :

$$\chi_{\text{vel}}^2 = \left[ \sum_{i,j} \frac{v(x_i, y_j) - v_{\text{model}}(x_i, y_j)}{\Delta v(x_i, y_j)} \right]^2. \quad (7)$$

In principle, all model parameters (disk center position, orientation and inclination, systemic velocity and dynamical mass) should be left free to vary. However, the moderate  $S/N$  of the data combined with the limited spatial coverage suggest to adopt a different approach in which some of these parameters are constrained a priori.

The mass distribution should be traced by the continuum flux distribution, therefore the disk center position should be identified by the continuum peak. Only in some objects we can detect continuum emission with high enough  $S/N$  to locate the disk center. In such cases we use that position in the fit allowing a variation of  $\pm 0.1''$  consistent with measurement errors. For all other objects we use the position inferred from the fitting of the emission line flux maps. For those objects where we detect a continuum component the average distance between line and continuum peaks is  $\sim 0.25''$ . Therefore, when we do not detect

any continuum, we allow for a variation of the disk center position of  $\pm 0.25''$ .

The scale radius of the mass distribution,  $r_e$ , cannot be derived from the velocity maps. Following [Cresci et al. \(2009\)](#), we fix  $r_e$  to the value of  $r_0$ , the scaling radius of the continuum flux map. When this is not detected, we adopt the scale radius of the emission line flux map. Estimating the scale radius  $r_e$  by fitting the IFD with a particular model (i.e. exponential) can of course lead to systematic errors. Therefore we will analyze for every object how systematic errors on  $r_e$  affect dynamical mass values.

Another potential source of systematic errors is the use of the line flux map to estimate disk center position and scale radius when no continuum is detected. Therefore we also evaluated how this choice affects the dynamical mass: for the objects where the continuum is detected we performed the fit of the velocity maps using the disk center position and scale radii estimated either from continuum and line flux maps. We find an average variation of 0.2 dex for the best fit  $M_{\text{dyn}}$  values. This can be considered an estimate of the systematic error associated to the use of the line flux map instead of the continuum one.

Since the disk inclination is coupled with the total dynamical mass, we decide to keep it as a fixed parameter in the fitting procedure to avoid convergence problems with the  $\chi^2$  minimization. Its best value and confidence interval is then identified by using a grid of  $i$  values and performing the fit for each of them. In this way we construct the  $\chi^2$  curve as a function of  $i$  which allows us to identify both the best  $i$  value and the confidence intervals (for details see [Avni 1976](#)). In the cases where the inclination is not constrained by the fit, we set its value to  $60^\circ$ , which represents the mean value for a population of uniformly randomly oriented disks.

#### 4.2.3. The intrinsic velocity dispersion

Our model computes the observed line velocity dispersion by taking into account the unresolved rotation, the intrinsic instrumental broadening ( $\sigma_{\text{spec}}$ ) and the broadening due to the finite size of the spatial pixels and of the spatial PSF. However, the disk can be characterized by an intrinsic velocity dispersion due to turbulent and non-gravitational motions in general. We estimate such intrinsic velocity dispersion of the gas as

$$\sigma_{\text{int}}(x_i, y_j)^2 = \max[(\sigma_{\text{observed}}(x_i, y_j)^2 - \sigma_{\text{model}}(x_i, y_j)^2); 0] \quad (8)$$

where  $\sigma_{\text{observed}}(x_i, y_j)$  is the observed map of velocity dispersion and  $\sigma_{\text{model}}(x_i, y_j)$  is that computed with the model which best fits the velocity map.

#### 4.2.4. Error estimates

To estimate the errors on the best fitting model parameters we use the bootstrap method ([Efron & Tibshirani 1994](#)). The dataset of each galaxy consists of  $n$  data points each characterized by spatial position, flux, velocity and velocity dispersion. We randomly extract from each dataset a subsample of  $n$  data points. Due to the random extraction, each subsample will have some data points that are replicated a few times and some data points that are entirely missing. We perform the fit on 100 subsamples and we then estimate errors on parameters by taking the standard deviation of the best fit values which are usually normally distributed.

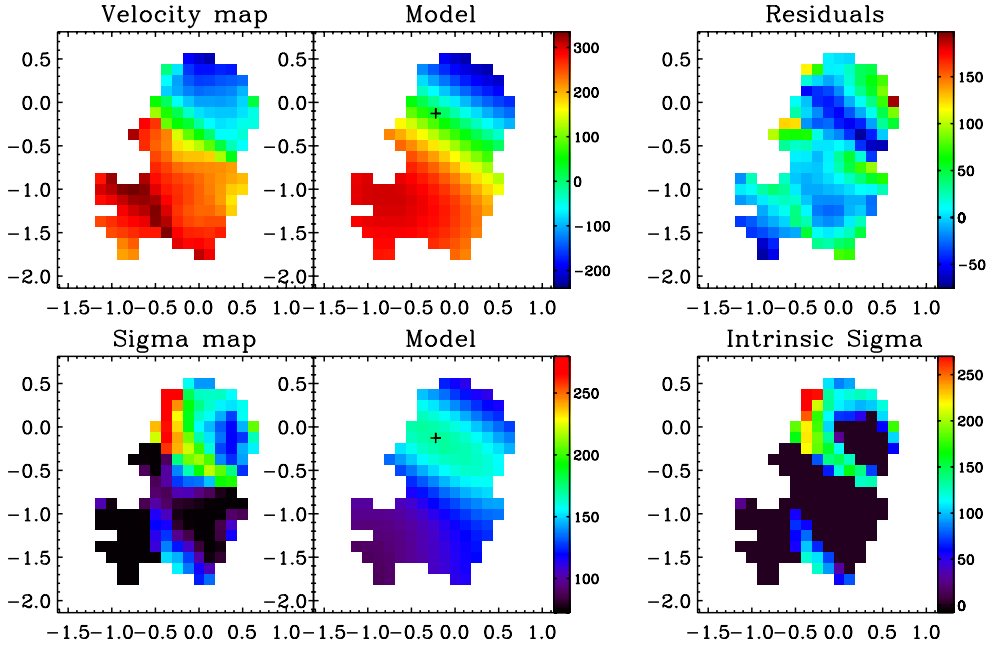


**Fig. 9.** Fit results for the object *SSA22A-M38*. Respectively on *top panels* from the left: data, model and residuals map. On *bottom panels* from the left: data, model and “intrinsic sigma” map. The plus sign on the middle panels represents the position of the model dynamical center. The  $X - Y$  coordinates are in arcsec referred to an arbitrary object center position. The north direction is the positive  $y$  axis. The vertical color bars are in  $\text{km s}^{-1}$ .

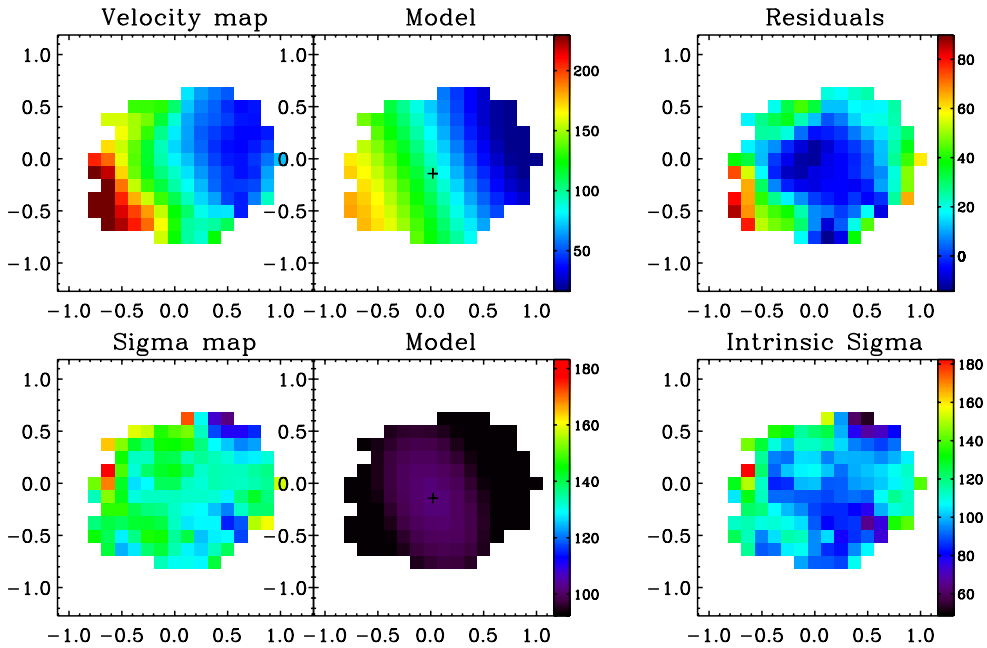


**Fig. 10.** Fit results for the object *SSA22A-C16*. Respectively on *top panels* from the left: data, model and residuals map. On *bottom panels* from the left: data, model and “intrinsic sigma” map. Axis, symbols color bars labels as in Fig. 9.

#### 4.3. Fit Results

The fit procedure outlined in the previous section is applied to the subsample of “rotating” objects in Table 2. In the following we present and discuss the results of the fit for each of these objects. The observed, model and residual velocity maps are presented in the top panels of Figs. 9–19. The bottom panels of the same figures show the observed and model and intrinsic velocity dispersion maps. The best fit parameters are presented in Table 3.

*SSA22a-M38* (Fig. 9). In this object, as shown in Fig. 1, we detect continuum emission which we use to estimate the position of the disk center. The inclination is constrained by the observations to  $i = 83^{+2}_{-1}$  at the  $1\sigma$  confidence level indicating that the disk is seen edge-on. This is a clear consequence of the fact that the observed iso-velocity contours do not show any curvature as expected when the rotating disk is seen at intermediate inclinations. The best fitting dynamical mass is then little affected by systematic errors due

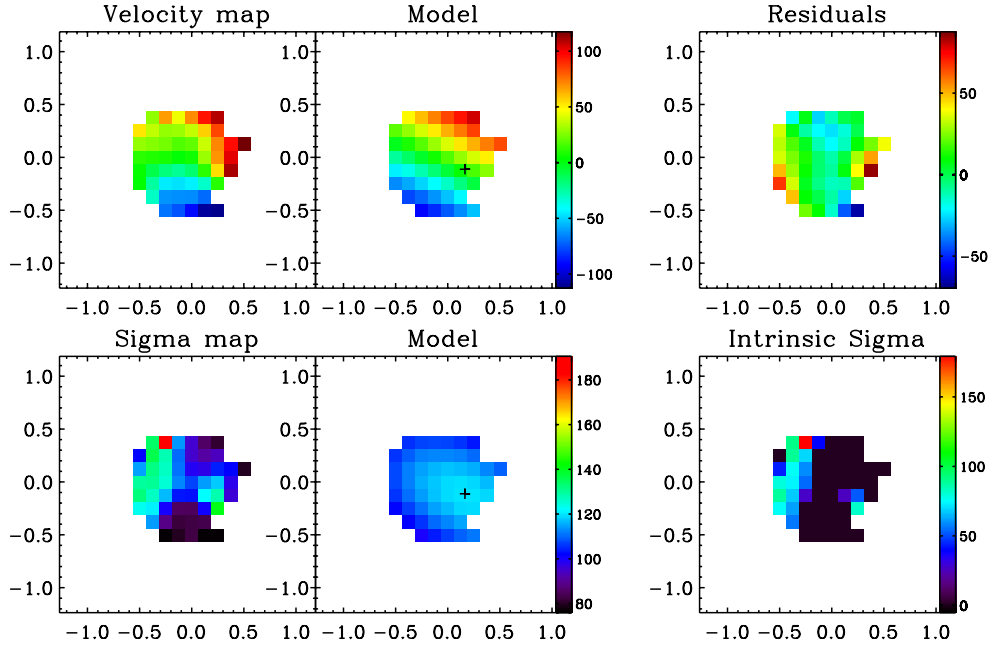


Fig. 11. Fit results for the object *CDFS-2528*. Panels, axis, symbols color bars labels as in Fig. 9.

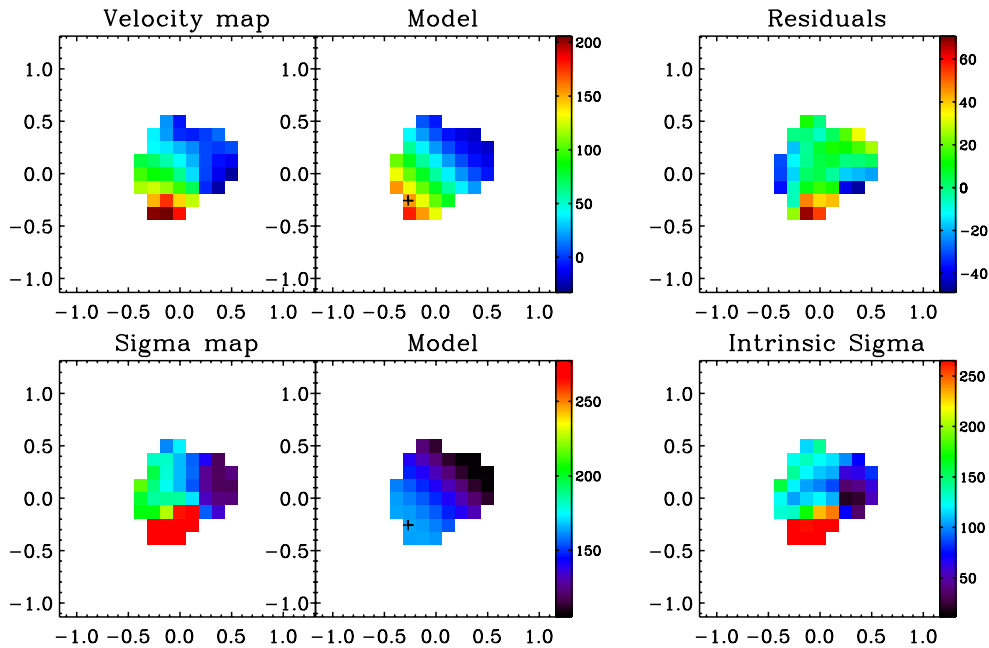


Fig. 12. Fit results for the object *SSA22a-D17*. Panels, axis, symbols color bars labels as in Fig. 9.

to uncertainties on the disk inclination. The *FWHM* of the spatial PSF estimated as described in Sect. 4.2.1 is  $0.5''$ . To evaluate how an incorrect estimate of this parameter can affect the  $M_{\text{dyn}}$  value we repeated the fit using *FWHM* in the range  $0.4\text{--}0.6''$ . The value of  $M_{\text{dyn}}$  differ in this case by only  $0.07$  dex. The characteristic radius  $r_e$  of each object depends on the value of the adopted PSF *FWHM* (e.g. setting a narrower PSF corresponds to an intrinsically broader flux distribution, with a greater  $r_e$ ). Therefore we have also evaluated how an incorrect estimate of the scale radius  $r_e$  affects the  $M_{\text{dyn}}$  best fit value. We repeated the fit using  $r_e$  different by

$\pm 30\%$  but keeping the PSF width fixed: the value of  $M_{\text{dyn}}$  changes by only  $\pm 0.1$  dex.

By adding in quadrature all the systematic errors we obtain the values for the systematic errors on the dynamical masses reported in Table 3.

In the bottom right panel of Fig. 9 we present the intrinsic velocity dispersion that is not accounted for by the ordered rotation of the gas. Most of the map is characterized by a very low intrinsic dispersion with average value of  $\langle \sigma_{\text{int}} \rangle \sim 50 \text{ km s}^{-1}$ . This means that most of the rotating disk is dynamically “cold”. However, a north-east region is apparently

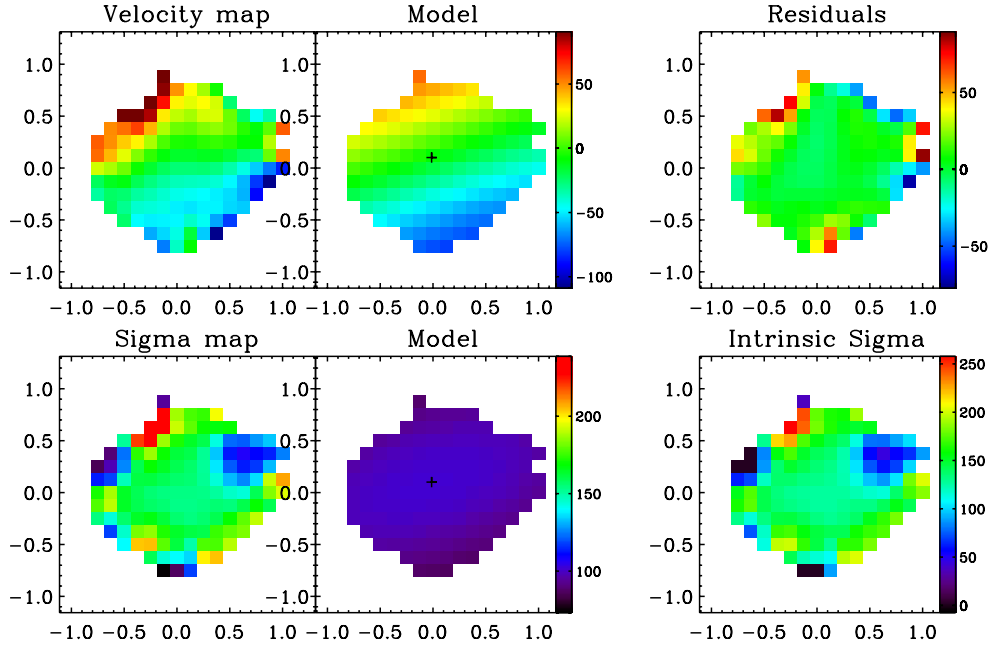


**Fig. 13.** Fit results for the object *CDFa-C9*. Panels, axis, symbols color bars labels as in Fig. 9.

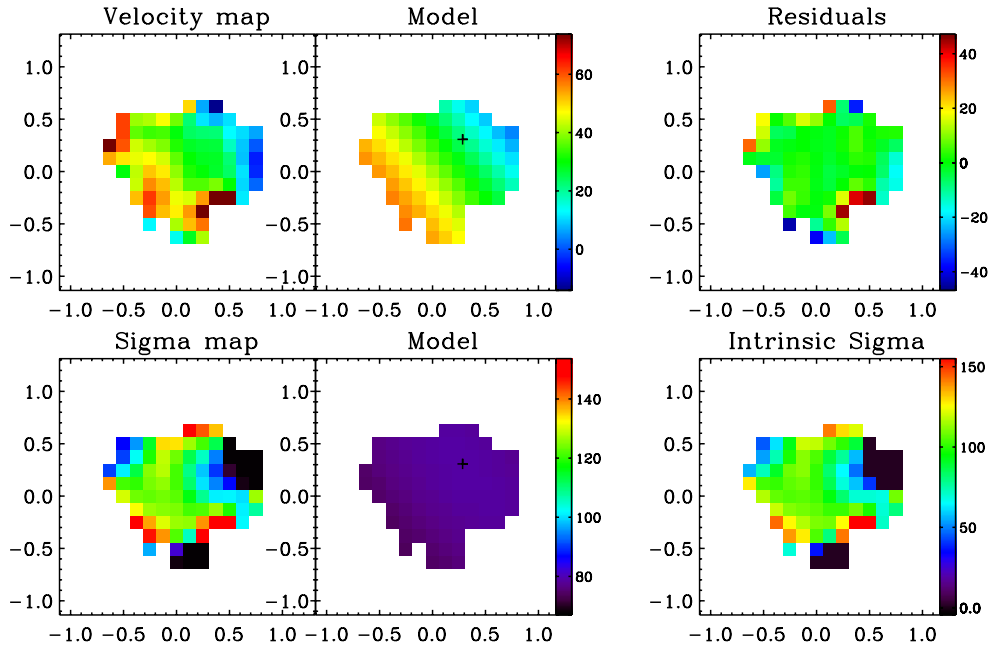


**Fig. 14.** Fit results for the object *CDFS-9313*. Panels, axis, symbols color bars labels as in Fig. 9.

characterized by high turbulence ( $\sigma_{\text{int}} \sim 250 \text{ km s}^{-1}$ ), although it is not clear whether the large velocity dispersion at this location is a consequence of low  $S/N$  of the emission lines. There is the possibility that the weak clump observable in the flux map at the south of the principal peak (Fig. 1) could be a distinct object. In our analysis we assume that all emission comes from an unique disk, but if the southern clump is really a distinct object we have to exclude its emission from the disk. However our assumption is strengthened by the continuum flux map that does not show any secondary clump, hence the secondary southern clump is likely a star forming region within the disk.

*SSA22a-C16* (Fig. 10). In this object we detect continuum emission that allows us to fix the center of rotation, but the  $S/N$  does not allow us to estimate the scaling radius, which is then inferred from the flux distribution of the emission line. The inclination is constrained to be  $i = 60^{+15}_{-30}$  at the  $1\sigma$  confidence level resulting in a systematic error on the mass of  $+0.45-0.03$  dex. The PSF width estimated is  $FWHM_{\text{PSF}} = 0.5''$ . Considering a range of variation of  $FWHM_{\text{PSF}} = 0.4-0.6''$ , the value of  $M_{\text{dyn}}$  has a systematic error of 0.15 dex. A variation of 30% of the disk scale radius produces a variation of 0.1 dex on the best fit  $M_{\text{dyn}}$  value. By combining all the contributions to the systematic error we

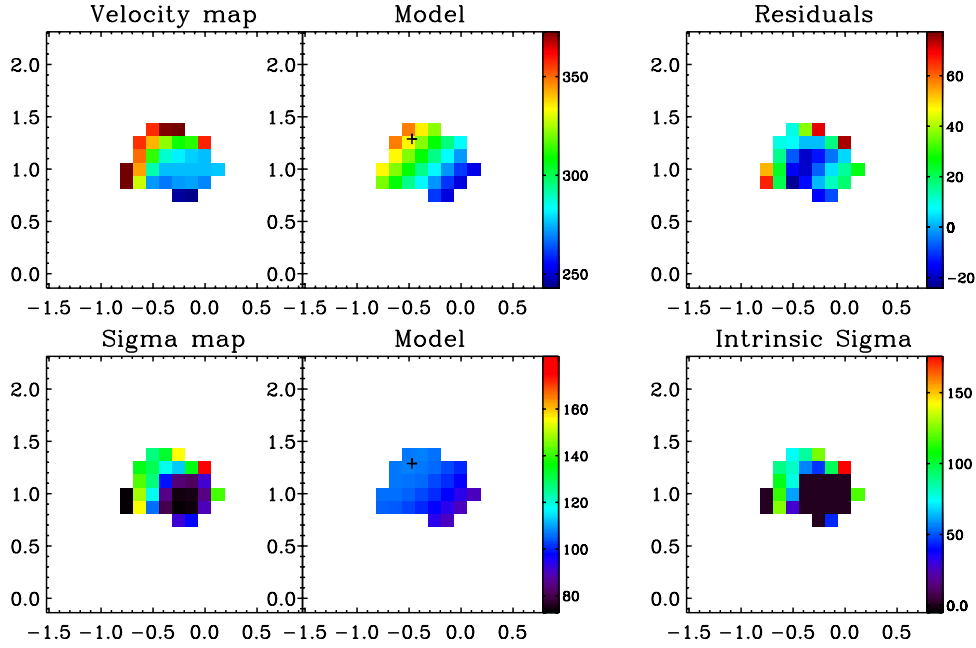


Fig. 15. Fit results for the object *CDFS-9340*. Panels, axis, symbols color bars indication same as in Fig. 9.

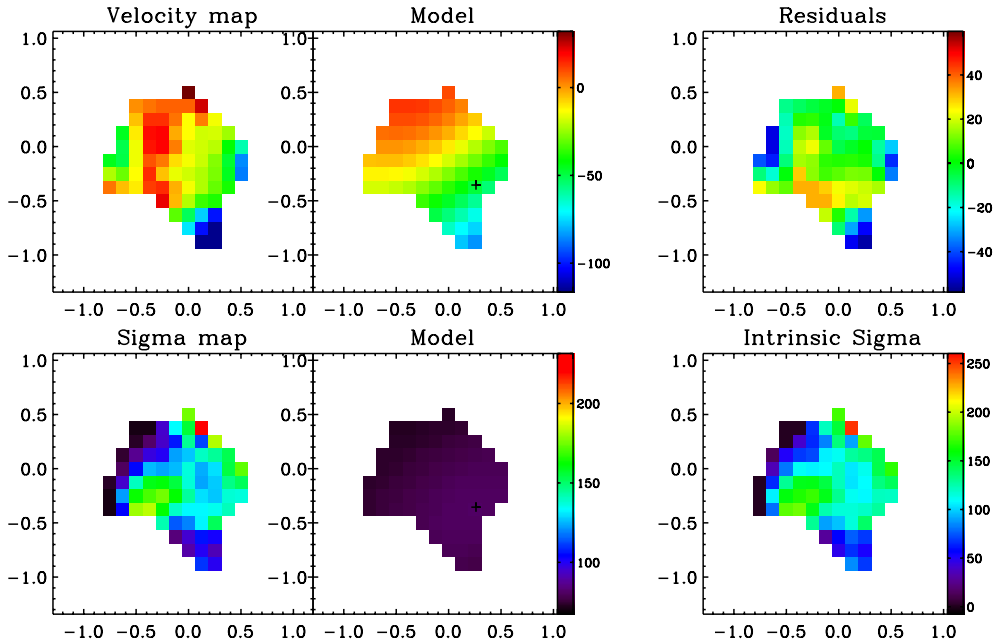


Fig. 16. Fit results for the object *3C324-C3*. Panels, axis, symbols color bars labels as in Fig. 9.

obtain a total error of  $+0.48-0.18$  dex. The intrinsic velocity dispersion maps in the bottom right panel of Fig. 10 indicates that this object is turbulent, with a quite constant value of  $\sigma_{\text{int}} \sim 100 \text{ km s}^{-1}$ .

*CDFS-2528* (Fig. 11). The continuum emission detected in this object can only be used to constrain the position of the center of rotation. The inclination is only constrained to be  $i < 70^\circ$ , therefore we can only provide a lower limit on the dynamical mass of  $\log(M_{\text{dyn}}/M_\odot) > 10.65$ . In this case, when inclination is partially or totally unconstrained, we estimate the mass by adopting the fiducial value of  $i = 60^\circ$ . The PSF estimated width is  $FWHM_{\text{PSF}} = 0.7''$ . Allowing a variation in

the range  $FWHM_{\text{PSF}} = 0.6-0.8''$  the value of  $M_{\text{dyn}}$  varies by 0.07 dex. A variation of 30% of the disk scale radius produces a variation on  $M_{\text{dyn}}$  of 0.1 dex. The intrinsic dispersion is quite low on average ( $\langle \sigma_{\text{int}} \rangle \sim 20 \text{ km s}^{-1}$ ) with an excess of  $\sim 100 \text{ km s}^{-1}$  in the East part.

*SSA22a-D17* (Fig. 12). For this object we do not detect any continuum emission. The inclination is constrained to be  $i > 70^\circ$  with a best fit value of  $85^\circ$ . The systematic error on the dynamical mass due to the inclination is then  $+0.02-0.13$  dex. The PSF width is  $FWHM_{\text{PSF}} = 0.65''$ . Varying  $FWHM_{\text{PSF}}$  by  $\pm 0.1''$  we find a negligible systematic error on the dynamical mass. Varying by 30% the disk scale radius produces a

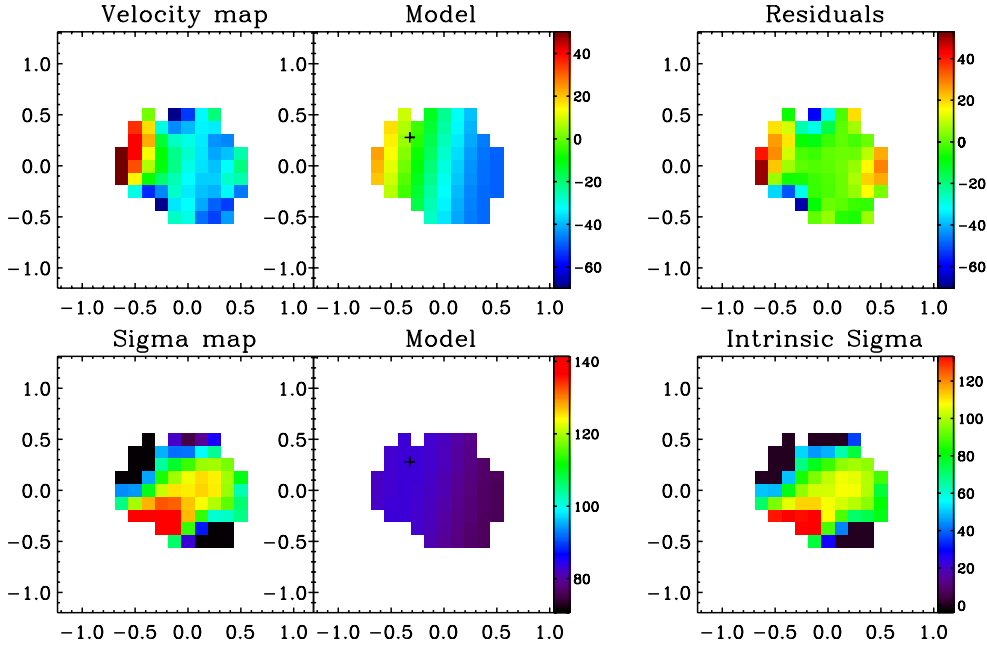


**Fig. 17.** Fit results for the object *CDFS-14411*. Panels, axis, symbols color bars labels as in Fig. 9.

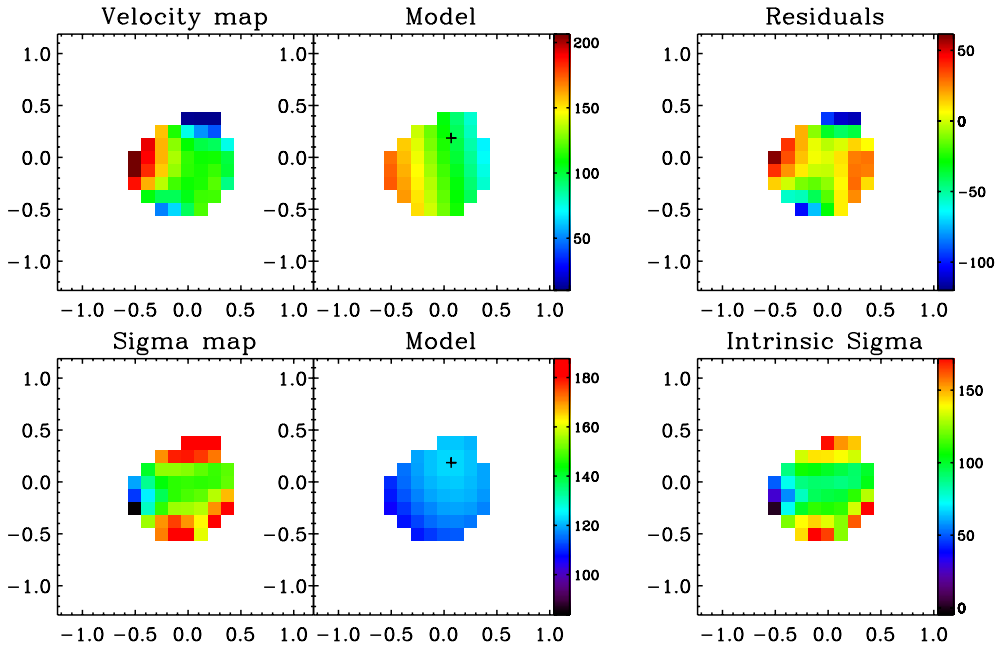


**Fig. 18.** Fit results for the object *CDFS-16767*. Panels, axis, symbols color bars labels as in Fig. 9.

variation on  $M_{\text{dyn}}$  of 0.08 dex. As previously noted, since we do not detect any continuum in this object we have to consider an additional systematic error of 0.2 dex due to the use of the line flux distribution. The disk is quite turbulent with an average intrinsic dispersion of  $\langle \sigma_{\text{int}} \rangle \sim 130 \text{ km s}^{-1}$  and a southern peak of  $\sim 250 \text{ km s}^{-1}$ .

*CDFa-C9* (Fig. 13). For this object we detect the continuum, but we can only constrain the disk center position. The inclination is constrained to be  $i > 20^\circ$  with a best fit value of  $60^\circ$ . The systematic error on the dynamical mass due to the inclination is then  $+0.8-0.1$  dex. The PSF width is  $FWHM_{\text{PSF}} = 0.5''$ . Varying  $FWHM_{\text{PSF}}$  by  $\pm 0.1''$  we find

a systematic error on  $M_{\text{dyn}}$  of 0.22 dex. Varying by 30% the disk scale radius produces a variation on  $M_{\text{dyn}}$  of only 0.02 dex, therefore we can neglect this contribution to the systematic error. The disk is quite turbulent with an average intrinsic dispersion of  $\langle \sigma_{\text{int}} \rangle \sim 120 \text{ km s}^{-1}$ .

*CDFS-9313* (Fig. 14). (In the same field as *CDFS-9340*). The continuum is not detected. We set the inclination to  $i = 60^\circ$  because it is totally unconstrained. The PSF width is  $FWHM_{\text{PSF}} = 0.7''$ . Varying  $FWHM_{\text{PSF}}$  by  $\pm 0.1''$  we find a  $M_{\text{dyn}}$  systematic error of 0.88 dex. Varying by 30% the disk scale radius produces a variation on  $M_{\text{dyn}}$  of only 0.02 dex, so we can neglect this contribution to the systematic error.

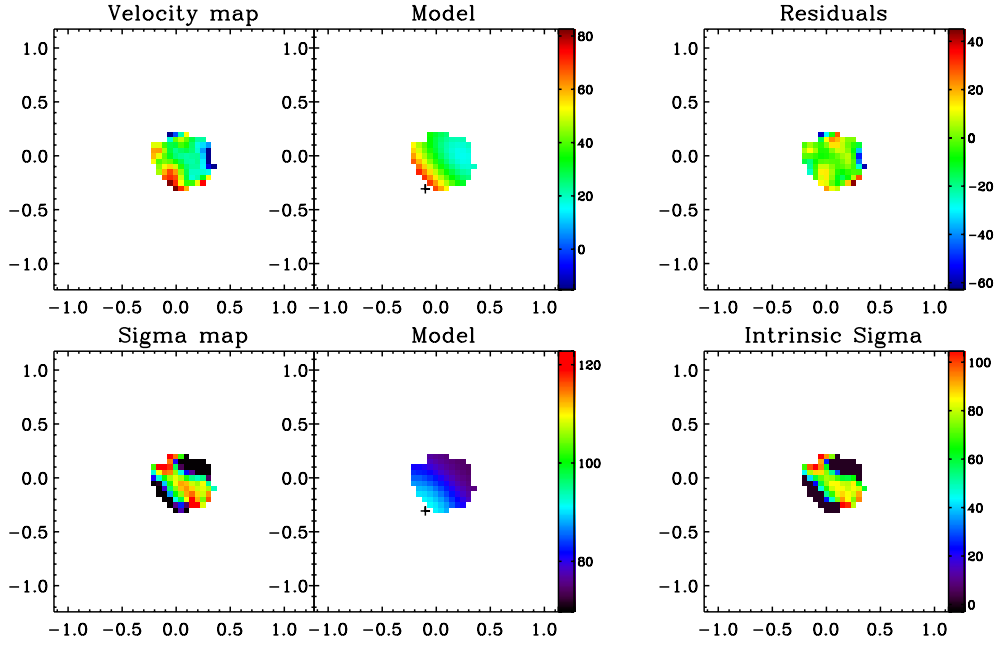


**Fig. 19.** Fit results for the object *Q0302-C131*. Panels, axis, symbols color bars labels as in Fig. 9.

**Table 3.** Fit results.

Object	$FWHM_{\text{PSF}} ["]$	Model parameter				
		$\theta [^\circ]$	$i [^\circ]^1$	$[\log_{10}(M_{\text{dyn}}/M_\odot)]$	$r_e [\text{kpc}]^2$	$V_{\text{max}} [\text{km s}^{-1}]$
SSA22a-M38	0.5	$149 \pm 2$	$83_{-1}^{+2}$	$11.34 \pm 0.02 (\pm 0.12)^3$	2.574	$346_{-45}^{+51}$
SSA22a-C16	0.5	$-111 \pm 2$	$60_{-30}^{+15}$	$10.31 \pm 0.02 (^{+0.48}_{-0.18})^3$	1.730	$129_{-24}^{+95}$
CDFS-2528	0.7	$-25 \pm 6$	$60 (<70)$	$10.71 \pm 0.05 (>10.65)^4$	1.644	$>197^4$
SSA22a-D17	0.65	$-45 \pm 5$	$80 (>70)$	$10.70 \pm 0.06 (^{+0.22}_{-0.25})^3$	1.214	$260_{-65}^{+75}$
CDFA-C9	0.5	$18 \pm 2$	$60 (>20)$	$9.93 \pm 0.03 (^{+0.83}_{-0.24})^3$	0.821	$129_{-31}^{+206}$
CDFS-9313	0.7	$128 \pm 4$	$60^5$	$9.29 \pm 0.04^5$	0.713	$67^5$
CDFS-9340	0.7	$44 \pm 12$	$70^5$	$10.3 \pm 0.1^5$	1.420	$151^5$
3C324-C3	0.7	$32 \pm 7$	$60_{-30}^{+10}$	$10.12 \pm 0.12 (^{+0.48}_{-0.23})^3$	2.5	$86_{-20}^{+63}$
CDFS-14411	0.6	$78 \pm 5$	$85_{-5}^{+3}$	$9.59 \pm 0.04 (\pm 0.21)^3$	1.240	$69_{-15}^{+19}$
CDFS-16767	0.55	$98 \pm 12$	$15^5$	$10.93 \pm 0.11^5$	0.362	$623^5$
Q0302-C131	0.3	$48 \pm 5$	$30 (<60)$	$9.99 \pm 0.07 (>9.59)^4$	0.466	$>117^4$

**Notes.** <sup>(1)</sup> Parameter hold fixed, confidence interval estimated as explained in the text. <sup>(2)</sup> Parameter hold fixed. <sup>(3)</sup> Systematic error. Obtained combining the systematic error contributes explained in the text. <sup>(4)</sup> Upper-lower limit. <sup>(5)</sup> Parameter unconstrained: we can not give a systematic error contribute due to this parameter.

The intrinsic velocity dispersion is quite constant over the entire map with an average value of  $\langle \sigma_{\text{int}} \rangle \sim 100 \text{ km s}^{-1}$ .

*CDFS-9340* (Fig. 15). (In the same field as *CDFS-9313*) The continuum is not detected. The inclination best fit value is  $i = 70^\circ$ , but it is unconstrained at the  $1\sigma$  confidence level. The PSF width is the same estimated for *CDFS-9313*. Varying  $FWHM_{\text{PSF}}$  by  $\pm 0.1''$  we find a  $M_{\text{dyn}}$  systematic error contribution of 0.1 dex. Varying by 30% the disk scale radius produces a variation on  $M_{\text{dyn}}$  of 0.1 dex. The intrinsic dispersion has an average value of  $\langle \sigma_{\text{int}} \rangle \sim 43 \text{ km s}^{-1}$ .

The small separation of this object from *CDFS-9313* either in position ( $\sim 1, 0'' - 7.2 \text{ kpc}$ ) and in redshift ( $\sim 280 \text{ km s}^{-1}$ ) suggests to consider them as an interacting pair. The most massive object is in this case the least luminous, *CDFS-9340*

(see Table 3). We estimate a mass ratio for the pair of  $\sim 10$ , indicative of a minor merging event with a relatively large separation of the two objects (i.e.  $\sim 7.2 \text{ kpc}$  compared to the disk scale radii of 0.7 kpc and 1.4 kpc), consistently with the non perturbed rotating disk kinematics observed in the two objects.

*3C324-C3* (Fig. 16). In this object we do not detect any continuum emission. The inclination is constrained to be  $30^\circ < i < 70^\circ$  with a best fit value of  $60^\circ$  providing a systematic error on the dynamical mass of  $+0.43-0.05$  dex. The PSF width is  $FWHM_{\text{PSF}} = 0.7''$ . Varying  $FWHM_{\text{PSF}}$  by  $\pm 0.1''$  we find a negligible  $M_{\text{dyn}}$  systematic error contribution (0.001 dex). Varying by 30% the disk scale radius results in a variation of  $M_{\text{dyn}}$  by 0.1 dex. We note that the observed velocity field

although showing a regular gradient is quite different from what expected in the case of a rotating disk. The intrinsic velocity dispersion is quite constant over the entire map with an average value of  $\langle\sigma_{\text{int}}\rangle \sim 125 \text{ km s}^{-1}$ .

**CDFS-14411** (Fig. 17). For this object we do detect a continuum emission and use it to constrain the disk center position and scale radius. The inclination is constrained to be  $80^\circ < i < 88^\circ$  with a best fit value of  $85^\circ$ . The dynamic mass systematic error due to the inclination is then negligible ( $\pm 0.04$  dex). The PSF width is  $FWHM_{\text{PSF}} = 0.6''$ . Varying  $FWHM_{\text{PSF}}$  by  $\pm 0.1''$  we find a  $M_{\text{dyn}}$  systematic error contribution of 0.17 dex. Varying by 30% the disk scale radius varies  $M_{\text{dyn}}$  by 0.12 dex. The intrinsic velocity dispersion rises in the center ( $\sigma_{\text{int}} \sim 110 \text{ km s}^{-1}$ ). The mean value over the entire map is  $\langle\sigma_{\text{int}}\rangle \sim 65 \text{ km s}^{-1}$ .

**CDFS-16767** (Fig. 18). In this object we detect the continuum emission and use it to constrain the disk center position and scale radius. The inclination best value is  $i = 15^\circ$ , but it is unconstrained at the  $1\sigma$  confidence level. The PSF width is  $FWHM_{\text{PSF}} = 0.55''$ . Varying  $FWHM_{\text{PSF}}$  by  $\pm 0.1''$  we find a  $M_{\text{dyn}}$  systematic error contribution of 0.21 dex. Varying of 30% the disk scale radius produces a negligible variation on  $M_{\text{dyn}}$  (0.04 dex). The disk is characterized by high turbulence with an average intrinsic dispersion of  $\langle\sigma_{\text{int}}\rangle \sim 100 \text{ km s}^{-1}$ .

**Q0302-C131** (Fig. 19). This is the only rotating object in the LSD sample. In this object we do not detect any continuum emission. The inclination is constrained to be  $i < 60^\circ$ , with a best fit value of  $30^\circ$  therefore we can only provide a lower limit on the dynamical mass of  $\log(M_{\text{dyn}}/M_\odot) > 9.59$ . The PSF width is  $FWHM_{\text{PSF}} = 0.3''$ . Varying  $FWHM_{\text{PSF}}$  by  $\pm 0.1''$  we find a  $M_{\text{dyn}}$  systematic error contribution of 0.88 dex. Varying by 30% the disk scale radius results in a negligible variation on  $M_{\text{dyn}}$  (0.01 dex). The disk has a quite low average intrinsic dispersion ( $\langle\sigma_{\text{int}}\rangle \sim 43 \text{ km s}^{-1}$ ).

## 5. Discussion

### 5.1. Rotating galaxies, turbulence and dynamical masses

In the AMAZE sample  $\sim 40\%$  of the galaxies show a smooth velocity gradient (10 out of 24) consistent with rotating disk kinematics. In the LSD sample only  $\sim 13\%$  of the galaxies show a smooth velocity gradient (1 out of 9). The smaller number of rotating objects in the LSD sample is likely due to the lower sensitivity of these observations to the outer, low surface brightness region (which dominate the “rotation signal”) because of the finer pixel scale, which makes the detector read-out noise more important relative to the AMAZE observations performed with larger pixel scale. Moreover, the AMAZE sample also tend to have a higher number of bright and redder targets (generally translating into higher masses), which may imply a higher fraction of “settled” massive systems. We note that the number of rotating galaxies is fully consistent, within statistical fluctuations, with that found in the SINS sample at  $z \sim 1.5\text{--}2.5$  ( $\sim 33\%$ ) (Förster Schreiber et al. 2009). This is particularly interesting, given that the latter sample includes not only rest-frame UV selected galaxies, but also near- and mid-IR selected, and that the fraction of rotating galaxies does not appear to depend on the selection criteria. Taken at face value, the comparison between the SINS analysis at  $z \sim 2$  and the AMAZE analysis at  $z \sim 3.3$  suggests that the fraction of rotating objects does not evolve within this redshift interval. Epinat et al. (2009) derive a fraction of rotating galaxies of 22% in a  $z \sim 1.2\text{--}1.6$  sample, but a direct comparison with this value is more difficult considering

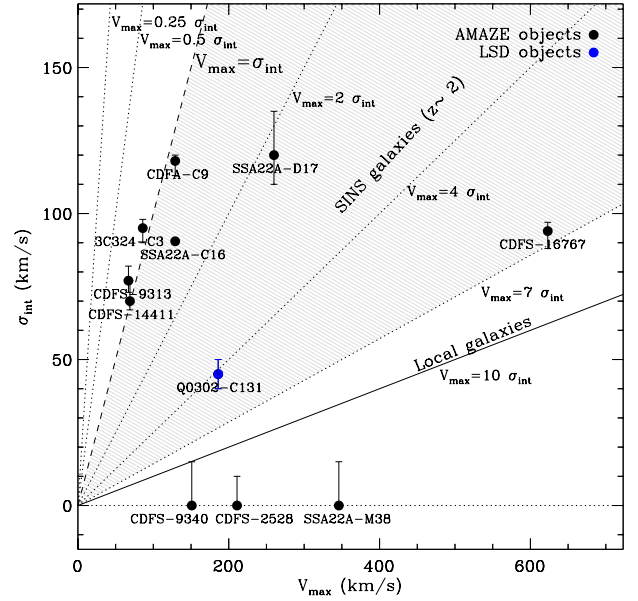


**Fig. 20.** Maximum rotational velocity  $V_{\text{max}}$  versus intrinsic velocity dispersion  $\sigma_{\text{int}}$ . Objects from the AMAZE and LSD samples are marked with black and blue symbols, respectively. The  $\sigma_{\text{int}}$  value is obtained fitting the observed velocity dispersion map and error bars represent  $1\sigma$  uncertainties. Overplotted the  $V_{\text{max}} = \sigma_{\text{int}}$  locus (dashed line), the  $V_{\text{max}} = k \sigma_{\text{int}}$  loci (dotted lines), the mean value of  $V_{\text{max}}/\sigma_{\text{int}}$  for the local galaxies (continuous line) and the  $V_{\text{max}}/\sigma_{\text{int}}$  interval for the SINS sample at  $z \sim 2$  (Förster Schreiber et al. 2009) (gray region).

that their definition of rotating objects is quite different from the one adopted here.

In any case, these results should be taken with great caution since several observational effects may easily affect the capability of identifying rotating objects. More specifically, the lack of angular resolution may prevent the detection of a rotation pattern or, vice versa, may blend two merging systems mimicking a rotation curve. Moreover, the limited sensitivity to low surface brightness disks (which is a strong function of redshift) may prevent us to identify large rotating disks in distant galaxies.

In the following we compare the ordered rotation (the velocity gradient  $\Delta v$  over the map) with the random motions (the mean velocity dispersion).

By using the results of our dynamical modeling we obtain the maximum rotational velocity ( $V_{\text{max}}$ ) and the intrinsic gas velocity dispersion  $\sigma_{\text{int}}$  (i.e. the turbulent gas motions). In Fig. 20 we plot  $V_{\text{max}}$  versus  $\sigma_{\text{int}}$  for our rotating objects.  $\sigma_{\text{int}}$  is a constant value added in quadrature to the model velocity dispersion and determined, as in Cresci et al. (2009), by fitting the observed velocity dispersion map. The line  $V_{\text{max}} = \sigma_{\text{int}}$  distinguish the loci of “rotation dominated” ( $V_{\text{max}} > \sigma_{\text{int}}$ ) and “dispersion dominated” objects ( $V_{\text{max}} < \sigma_{\text{int}}$ ) and, for comparison, in local disk galaxies  $V_{\text{max}}/\sigma_{\text{int}} \sim 10$ . From Fig. 20 it is clear that, with  $V_{\text{max}}/\sigma_{\text{int}} < 2$ , the majority of the rotating galaxies at  $z \sim 3$  (6 out of 11) is composed of dynamically “hot” disks, in contrast with local galaxies. Two galaxies have a higher  $V_{\text{max}}/\sigma_{\text{int}}$  ratio but still lower than local galaxies, while three galaxies are dynamically “cold”. The finding that high- $z$  disk galaxies are much more turbulent than local galaxies was already obtained by other studies at  $z \sim 1\text{--}2$  (e.g. Genzel et al. 2006; Förster Schreiber et al. 2006) and is suggestive of high gas fractions making disks gravitationally unstable (Tacconi et al. 2010;

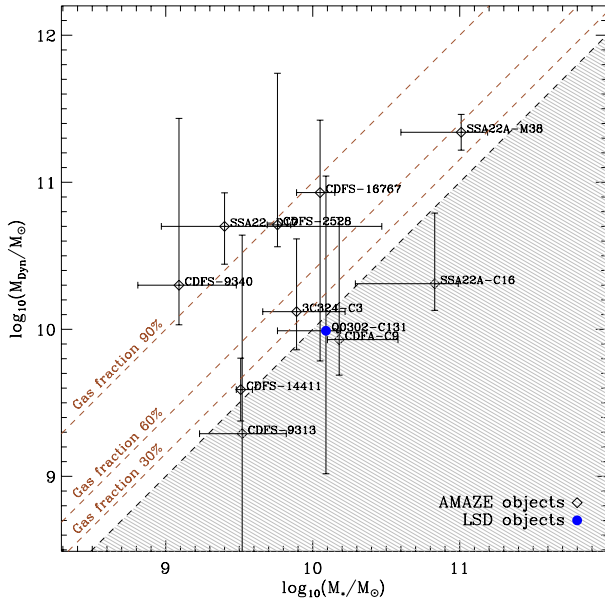


**Fig. 21.** Comparison of the dynamical and stellar mass for the objects analyzed in this paper. The masked gray region represents the non-physical condition of  $M_* > M_{\text{dyn}}$ . The brown dashed lines represent the loci of constant gas fraction (90%, 60% and 30% gas fraction, from left to right, respectively).

Daddi et al. 2010a). Förster Schreiber et al. (2009) obtain with the SINS sample  $V_{\text{max}}/\sigma \sim 1-7$  with a mean value of 4.5. Our result at  $z \sim 3.3$  ( $\langle V_{\text{max}}/\sigma_{\text{int}} \rangle_{z=3.3} \sim 2$ ) goes in the same direction and is even more extreme considering that the majority of our galaxies have  $V_{\text{max}}/\sigma_{\text{int}}$  comparable with the lowest values observed in the SINS survey. We do find however a few galaxies which are dynamically “cold” even when compared to local galaxies. The missing link between high redshift and local galaxies seems to be provided by Epinat et al. (2009) who obtain  $\langle V_{\text{max}}/\sigma_{\text{int}} \rangle \sim 3.5$  (at  $z \sim 1.2-1.6$ ) when considering the objects classified as “rotating disks” and “perturbed rotators”. This number rises to 7.2 when considering only the “rotating disks”.

In Fig. 21 we compare dynamical and stellar masses for the rotating objects. We estimate dynamical masses in the range  $\sim 1.8 \times 10^9 M_{\odot} - 2.2 \times 10^{11} M_{\odot}$  with a mean value of  $1.6 \times 10^{10} M_{\odot}$ . The stellar masses are reported in Table 4 and are estimated from standard broad-band SED fitting (see Sect. 6 of Maiolino et al. 2008a; and Sect. 4.3 of Mannucci et al. 2009, for more details).

All of the objects are consistent with having stellar masses lower than dynamical masses within the  $1\sigma$  uncertainties. By ascribing the difference between dynamical and stellar mass to the gas mass, the loci of constant gas fraction are given by the dashed lines. Here we are assuming negligible contribution of Dark Matter, justified by the fact that the spatial region sampled in our dynamical study is only 2–3 characteristic radii of the exponential disk, where the contribution of dark matter is still small. In any case, if this assumption is not appropriate, we can call this quantity a “gas and dark matter” fraction. Three objects require at high confidence a gas fraction of 90% or higher. One object (SSA22a-C16) has little room for any gas mass. Most of the other galaxies have the gas fraction poorly constrained or totally unconstrained, except for SSA22a-M38 (with a gas fraction constrained within 30% and 80%) and CDFS-14411 (with a gas fraction constrained to  $<40\%$ ). However, due to the high uncertainties, it is not possible to draw firm conclusions on the

**Table 4.** Stellar masses and star formation rates.

Object	$[\log_{10}(M_*/M_{\odot})]$	$SFR [M_{\odot}/y]$
SSA22a-M38	$11.01^{+0.18}_{-0.41}$	$115^{+0}_{-0}$
SSA22a-C16	$10.83^{+0.16}_{-0.54}$	$651^{+0}_{-0}$
CDFS-2528	$9.76^{+0.09}_{-0.07}$	$101^{+5.9}_{-53.8}$
SSA22a-D17	$9.40^{+1.07}_{-0.43}$	$45.1^{+0}_{-0}$
CDFS-9313	$9.52^{+0.29}_{-0.28}$	$31.3^{+29.4}_{-23.9}$
CDFS-9340	$9.09^{+0.39}_{-0.28}$	$11.7^{+11}_{-9.1}$
3C324-C3	$9.95^{+0.37}_{-0.18}$	$88.6^{+68.8}_{-78.6}$
CDFS-14111	$9.51^{+0.08}_{-0.03}$	$71^{+8.1}_{-3.8}$
CDFS-16767	$10.06^{+0.10}_{-0.16}$	$84^{+89.1}_{-9.1}$
Q0302-C131	$10.09^{+0.10}_{-0.33}$	$10^{+6}_{-4}$

observed wide range of gas fractions, and more data are needed to set tighter constraints on this property.

It is interesting to compare the amount of gas inferred from the comparison between dynamical and stellar mass with the amount of gas that can be inferred from the Schmidt-Kennicutt law. More specifically, if we assume the validity of the Schmidt-Kennicutt law (hereafter SK) for our  $z \sim 3$  galaxies, we can calculate the gas surface density from the star formation rate surface density, and therefore derive the gas mass. In particular we use the relation presented in Mannucci et al. (2009) (Eqs. (1) and (2)) that adopt for the slope of the SK relation the value 1.4 given by Kennicutt (1998). To infer the SFR surface density we use the characteristic radius of the mass distribution  $r_e$  estimated in our dynamical modeling as the radius of the galaxy. Then, under the assumption of a negligible contribution in mass of the dark matter, and by adding the stellar mass to the gas mass we obtain the baryonic mass of the galaxy ( $M_{\text{bar}}$ ). In this way we obtain for our objects an estimate of the mass by using only the results of the SED fitting.

In Fig. 22 we show the comparison of the  $M_{\text{dyn}}$  estimated from the gas dynamics modeling presented in this paper and the  $M_{\text{bar}}$  estimated from the SK law, combined with the stellar mass. The two estimates of the mass, considering the error bars, are generally quite consistent. The mean difference (in module) (i.e. the mean scatter of the points around the  $M_{\text{dyn}} = M_{\text{bar}}$  condition) is of  $\sim 0.5$  dex and there is no particular bias of one of the two values on respect of the other. The mean residual of the points on respect of the  $M_{\text{dyn}} = M_{\text{bar}}$  condition (i.e. the difference in module divided by the errors) is  $\sim 1.2$ . We can conclude that the results of the SED fitting give a reliable estimate of the dynamical mass. This also implies that the two assumptions of the validity of the SK law and of a negligible contribution in mass of the dark matter appear to be valid.

Daddi et al. (2010b) using CO observations of galaxy samples at low and high redshifts ( $z \sim 0.5$  and  $z \sim 1.5$ ) find a 1.42 slope for the SK relation, very similar to that by Kennicutt (1998). Genzel et al. (2010) using systematic data sets of CO molecular line emission in  $z \sim 1-3$  normal star-forming galaxies find instead an index of  $\sim 1.1-1.2$ . In the present work we have used the Kennicutt (1998) index for comparison with other data in the literature, but using the smaller Genzel et al. (2010) index we would have obtained, on average, gas masses higher by only  $\sim 0.3$  dex.

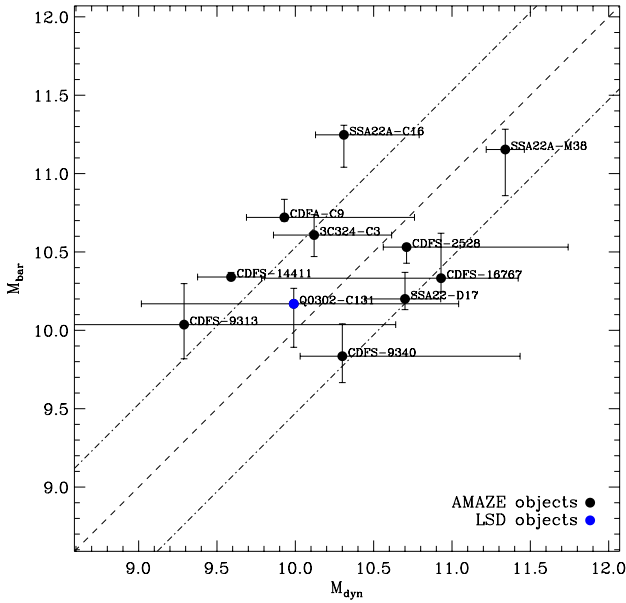


**Fig. 22.** Comparison of the dynamical mass  $M_{\text{dyn}}$  obtained from the gas dynamical modeling and the baryonic mass  $M_{\text{bar}}$  obtained by combining the stellar mass and the gas mass inferred from the SK law. The dashed line represents the condition of equality of the two masses. The dot-dashed lines represents the mean scatter of the points around the  $M_{\text{dyn}} = M_{\text{bar}}$  condition ( $\sim 0.5$  dex).

## 5.2. The Tully-Fisher relation at $z \sim 3$

The Tully-Fisher relation (hereafter TFR) is the relation between luminosity (or stellar mass) and maximum rotational velocity of disk galaxies (Tully & Fisher 1977). This relation, originally used as a distance indicator for disk galaxies, represents an important feature for understanding galaxy formation and evolution because it links directly the angular momentum of the dark matter halo with the stellar mass content of disk galaxies. In fact, according to theoretical models, galaxy disks form out of gas cooling down from a surrounding dark matter halo, maintaining its specific angular momentum and settling in a rotationally supported disk. Therefore, the structure and dynamics of disk galaxies at different cosmic epochs are expected to be closely correlated with the properties of the dark matter halo in which they are embedded.

In recent years, an increasing number of dynamical studies of disk galaxies in the local and intermediate-redshift Universe allowed the investigation of the evolution of the TFR with redshift.

The evolution of the TFR is expected to be related both to the conversion of gas into stars and to the inside-out growth of the dark matter halo by accretion. In fact, while the extent of the halo grows considerably with time, the circular velocity of the halo grows less, keeping the rotation curve approximately flat to longer and longer distances. The accretion of the dark matter is followed by accretion of baryonic gas, which is subsequently converted into stars by ordinary star formation in the disk. However, the details of the process and the amount of evolution expected depends strongly on the model assumptions, on the accretion mechanism and the timescale needed to convert the gas into stars. Any successful model of disk formation should then be able to reproduce the slope, zero-point, scatter, and redshift evolution of the TFR.

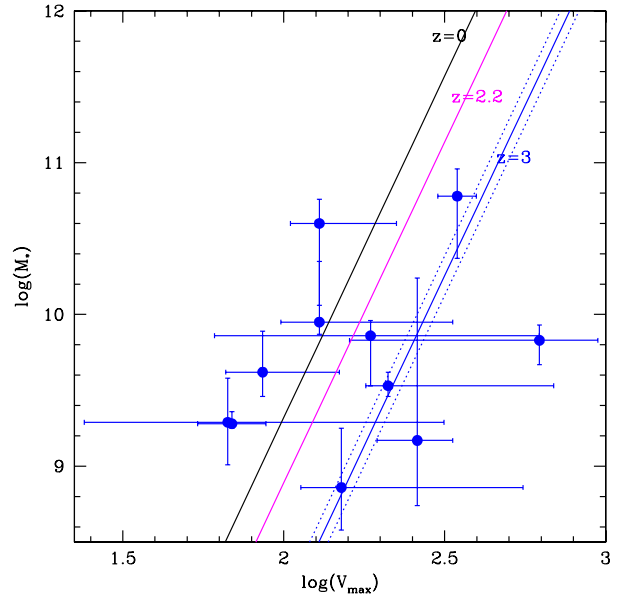


**Fig. 23.** The Tully-Fisher relation at  $z \sim 3$  reconstructed by using the dynamical and stellar masses of the rotating galaxies found in our sample. The solid black line represents the local relation, the magenta line represents the  $z \sim 2$  relation (Cresci et al. 2009) and blue solid line represents the fit to our data ( $z \sim 3$ ) by keeping the same slope as for the local and  $z \sim 2$  cases. The dotted blue lines represents the formal  $1\sigma$  uncertainty on the zero point of our fitted relation.

There are still discrepant results on a possible evolution at intermediate redshifts of the tight relation observed in local galaxies (e.g., Haynes et al. 1999; Pizagno et al. 2007). For example Vogt et al. (1996) reported very little evolution of the B-band TFR up to  $z \sim 1$ , but other groups (e.g. Barden et al. 2003; and Nakamura et al. 2006) found a strong brightening of  $\sim 1-2$  mag in B-band luminosity over the same redshift range.

Furthermore, the interpretation of a possible evolution of the luminosity TFR is difficult since the luminosity and the angular momentum might be evolving together. As a consequence, the stellar mass TFR, which correlates the stellar mass and the maximum rotational velocities of disks, offers a physically more robust comparison as it involves more fundamental quantities.

In this context, Flores et al. (2006), Kassin et al. (2007), and Conselice et al. (2005) have found no evolution in both the slope and zero point of the stellar mass TFR up to  $z = 1.2$ .

In contrast Puech et al. (2008) detect an evolution of the TFR zero point of 0.36 dex between  $z \sim 0.6$  and  $z = 0$ , by using a sample of 18 disk like galaxies observed with the integral-field spectrograph GIRAFFE at the VLT.

At  $z \sim 2$  Cresci et al. (2009) build a TFR based on the SINS sample and find an evolution of the TFR zero point of  $\sim 0.4$  dex relative to the local TFR.

By using the dynamics of  $z \sim 3$  galaxies inferred from our data, we are now able to derive the TFR at  $z \sim 3$ . In Fig. 23 we present the  $z \sim 3$  TFR obtained by using the data presented in this paper (obviously only for the rotating objects). The maximum rotational velocities have been computed from the best fit models as reported in Table 3. The stellar masses are those reported in Table 4.

All our data points are consistent with having a stellar-to-dynamical mass ratio smaller than the local value. We can

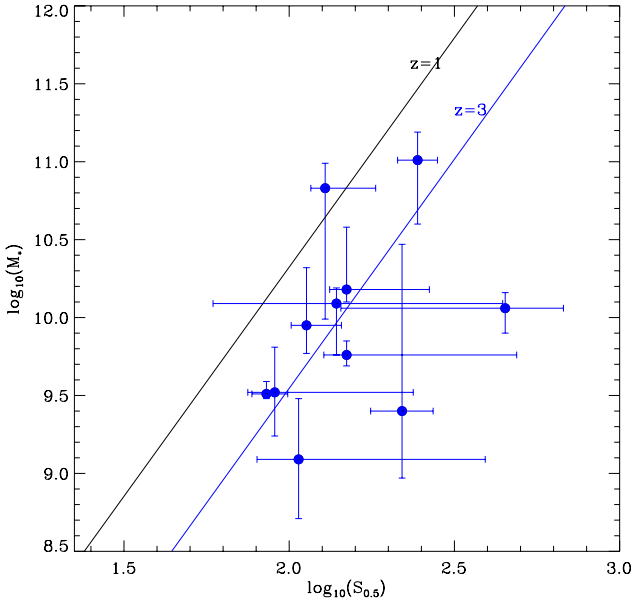


**Fig. 24.** The  $S_{0.5}$  Tully-Fisher relation at  $z \sim 3$ . The solid black line represents the  $z \sim 1$  relation (Kassin et al. 2007), the dashed line represents the fit to our data ( $z \sim 3$ ) by keeping the same slope as for the  $z \sim 1$  relation.

actually observe an evolution of the TFR with the redshift and this evolution is in the direction predicted by the models: the dynamical mass is already in place at this cosmic epoch, but the stellar mass has yet to be formed.

The large scatter ( $\sim 1.5$  dex) of the TFR at  $z \sim 3$  suggests that at this redshift the relation is not yet in place, probably due to the young age of the galaxies at this epoch (between 50 Myr and 500 Myr). However we can not exclude that our  $V_{\max}$  measurements are affected by an incorrect assumption of a rotating disk kinematics for some objects of our samples, which introduces a large scatter in the relation.

Assuming that the TFR is in place, despite the large data scatter, and that the slope is the same of the local universe, we can fit the relation obtaining a zero point for our data of  $-0.97 \pm 0.13$ . This implies an evolution of the zero point of 1.29 dex relative to the local TFR and 0.88 dex relative to the  $z \sim 2$  TFR.

Given the high intrinsic velocity dispersion observed in our  $z \sim 3$  sample, we also explored the  $S_{0.5} = \sqrt{0.5V^2 + \sigma^2}$  estimator introduced by Kassin et al. (2007) to study the impact of turbulent motions. In Fig. 24 we present the  $S_{0.5}$  TFR obtained by using our  $V_{\max}$  and  $\sigma_{\text{int}}$  values. Kassin et al. (2007) found a tight relation ( $\sim 0.3$  dex scatter in  $M_{*}$ ) in a sample of galaxies with redshift up to  $z = 1.2$ , with no significant evolution. By only allowing for a change in zero point of the  $z \sim 1$  relation we estimate a mean scatter of  $\sim 0.5$  dex in our galaxies at  $z \sim 3.3$ . The reduction of the scatter in the  $S_{0.5}$  TFR compared to the classical one ( $\sim 1.5$  dex) suggests that, at least for some objects, part of the mass might be supported by turbulent or not ordered motions. We observe a significant evolution of the zero point of the relation between  $z \sim 1$  and  $z \sim 3$  ( $\sim 0.8 \pm 0.1$  dex in  $M_{*}$ ), providing further support for the observed evolution on the classical TFR.

The use of SINFONI integral-field spectra represents a major step forward in the modeling of the dynamics of high- $z$  galaxies, as the two-dimensional mapping is more complete and not biased by a priori assumptions about the kinematic major axis

and inclination of the system as in long-slit spectroscopy. Also SINFONI data can allow a better selection of the rotating systems and ensure a much lower contamination from complex dynamics and irregular motions than in longslit data sets. This might be a reason for the apparent inconsistency of the results of kinematical studies at redshift greater than 0.5.

## 6. Conclusions

We conducted an extensive investigation of the dynamics of  $z \sim 3$  galaxies using near infrared integral-field spectra obtained with SINFONI at the ESO VLT. This is the first time that such dynamical analysis is conducted for a relatively large sample (33 galaxies) at  $z \sim 3$ .

- We estimated galaxy masses by fitting rotating disk models to selected galaxies. Due to the relatively low  $S/N$  of the data, we implemented a simple but quantitative method to identify smooth velocity gradients, which are the signature of possible disk rotation. After this pre-selection, we performed complete dynamical modeling using a rotating disk model with an exponential mass profile.
- We found that the kinematics of  $\sim 30\%$  of the objects (11 out of 33) is consistent with that of a rotating disk. This number is fully consistent with that found with  $z \sim 2$  samples, like SINS, suggesting that the number of rotating objects does not evolve between  $z \sim 2$  and 3.
- When considering only the galaxies observed with AO and finer pixel scale (LSD sample), only 1 out of 9 shows a smooth velocity gradient. This is likely the consequence of such observational setup providing higher spatial resolution but lower sensitivity to the outer, low surface brightness regions which dominate the “rotation signal”.
- The 11 rotating objects have dynamical masses in the range  $\sim 1.8 \times 10^9 M_{\odot} - 2.2 \times 10^{11} M_{\odot}$  with a mean value of  $\sim 1.6 \times 10^{10} M_{\odot}$ .
- By comparing the amplitude of the inclination-corrected velocity gradient with the intrinsic gas velocity dispersion derived from models, we found that the majority of the rotating galaxies at  $z \sim 3$  are dynamically “hot” disks with an average  $\langle \Delta v_{\text{deproj}} / \sigma_{\text{int}} \rangle \sim 2$ . This confirms the results obtained by other studies at  $z \sim 1-2$  ( $\Delta v / \sigma \sim 2-4$ ), indicating that high- $z$  disk galaxies are more turbulent than local galaxies and even more “hot” than galaxies at  $z \sim 2$ .
- We compared stellar and dynamical masses for the rotating objects, and derived an estimate of the “gas and dark matter” fraction. Using independent estimates for stellar mass and star formation rate, and applying the Schmidt-Kennicutt law, we obtained a SED-based estimate of the total baryonic mass of our objects. This estimate is consistent with our estimate of the mass from gas dynamics (rms scatter lower than 0.5 dex). This shows that SED fitting gives a reliable estimate of the dynamical mass and also implies that our assumptions on the validity of the SK law and of a negligible contribution of dark matter are justified.
- Finally, we obtained the Tully-Fisher relation at  $z \sim 3$ . All our data points are consistent with a stellar-to-dynamical mass ratio smaller than the value in the local universe confirming the redshift evolution of the relation already found at  $z \sim 2$ . This is consistent with models predictions, according to which stellar mass is still building up compared to the total dynamical mass. However, the large scatter of the points may also suggest that, at this redshift, the relation is not yet in place, probably due to the young age of the galaxies. The

Tully-Fisher relation based on the  $S_{0.5}$  indicator has a significantly lower scatter than the “classical” one and also shows an evolution in zero point compared to  $z \sim 1$ . The reduction in scatter suggests that, at least for some objects, part of the mass might be supported by turbulent motions.

*Acknowledgements.* We wish to thank the referee for his/her really thorough and constructive report on this paper. This work was partly funded by INAF and ASI through contract ASI-INAF I/016/07/0 and by the Marie Curie Initial Training Network ELIXIR of the European Commission under contract PITN-GA-2008-214227.

## References

- Avni, Y. 1976, *ApJ*, 210, 642
- Barden, M., Lehnert, M. D., Tacconi, L., et al. 2003, unpublished [arXiv:astro-ph/0302392]
- Binney, J., & Tremaine, S. 1987, *Galactic dynamics* (Princeton University Press)
- Blumenthal, G. R., Faber, S. M., Primack, J. R., & Rees, M. J. 1984, *Nature*, 311, 517
- Conselice, C. J., Bundy, K., Ellis, R. S., et al. 2005, *ApJ*, 628, 160
- Conselice, C. J., Bundy, K., Trujillo, I., et al. 2007, *MNRAS*, 381, 962
- Cresci, G., Hicks, E. K. S., Genzel, R., et al. 2009, *ApJ*, 697, 115
- Cresci, G., Mannucci, F., Maiolino, R., et al. 2010, *Nature*, 467, 811
- Daddi, E., Bournaud, F., Walter, F., et al. 2010a, *ApJ*, 713, 686
- Daddi, E., Elbaz, D., Walter, F., et al. 2010b, *ApJ*, 714, L118
- Davis, M., Efstathiou, G., Frenk, C. S., & White, S. D. M. 1985, *ApJ*, 292, 371
- Dickinson, M., Papovich, C., Ferguson, H. C., & Budavári, T. 2003, *ApJ*, 587, 25
- Efron, B., & Tibshirani, R. J. 1994, *An Introduction to the Bootstrap* (Chapman & Hall/CRC)
- Eisenhauer, F., Abuter, R., Bickert, K., et al. 2003, in *SPIE Conf. Ser.* 4841, ed. M. Iye, & A. F. M. Moorwood, 1548
- Epinat, B., Contini, T., Le Fèvre, O., et al. 2009, *A&A*, 504, 789
- Erb, D. K., Steidel, C. C., Shapley, A. E., et al. 2006, *ApJ*, 646, 107
- Flores, H., Hammer, F., Puech, M., Amram, P., & Balkowski, C. 2006, *A&A*, 455, 107
- Förster Schreiber, N. M., Genzel, R., Lehnert, M. D., et al. 2006, *ApJ*, 645, 1062
- Förster Schreiber, N. M., Genzel, R., Bouché, N., et al. 2009, *ApJ*, 706, 1364
- Genzel, R., Tacconi, L. J., Eisenhauer, F., et al. 2006, *Nature*, 442, 786
- Genzel, R., Burkert, A., Bouché, N., et al. 2008, *ApJ*, 687, 59
- Genzel, R., Tacconi, L. J., Gracia-Carpio, J., et al. 2010, *MNRAS*, 407, 2091
- Grazian, A., Salimbeni, S., Pentericci, L., et al. 2007, *A&A*, 465, 393
- Haynes, M. P., Giovanelli, R., Salzer, J. J., et al. 1999, *AJ*, 117, 1668
- Hopkins, A. M., & Beacom, J. F. 2006, *ApJ*, 651, 142
- Jones, T. A., Swinbank, A. M., Ellis, R. S., Richard, J., & Stark, D. P. 2010, *MNRAS*, 404, 1247
- Kassin, S. A., Weiner, B. J., Faber, S. M., et al. 2007, *ApJ*, 660, L35
- Kennicutt, Jr., R. C. 1998, *ApJ*, 498, 541
- Krajinović, D., Cappellari, M., de Zeeuw, P. T., & Copin, Y. 2006, *MNRAS*, 366, 787
- Law, D. R., Steidel, C. C., Erb, D. K., et al. 2007, in *Amer. Astron. Soc. Meet. Abstr.*, 211
- Law, D. R., Steidel, C. C., Erb, D. K., et al. 2009, *ApJ*, 697, 2057
- Lemoine-Busserolle, M., Bunker, A., Lamareille, F., & Kissler-Patig, M. 2010, *MNRAS*, 401, 1657
- Maiolino, R., Nagao, T., Grazian, A., et al. 2008a, *A&A*, 488, 463
- Maiolino, R., Nagao, T., Grazian, A., et al. 2008b, in *ASP Conf. Ser.* 396, ed. J. G. Funes, & E. M. Corsini, 409
- Mannucci, F., & Maiolino, R. 2008, in *IAU Symp.* 255, ed. L. K. Hunt, S. Madden, & R. Schneider, 106
- Mannucci, F., Buttery, H., Maiolino, R., Marconi, A., & Pozzetti, L. 2007, *A&A*, 461, 423
- Mannucci, F., Cresci, G., Maiolino, R., et al. 2009, *MNRAS*, 398, 1915
- Mannucci, F., Cresci, G., Maiolino, R., Marconi, A., & Gnerucci, A. 2010, *MNRAS*, 1314
- Marconi, A., Axon, D. J., Capetti, A., et al. 2003, *ApJ*, 586, 868
- Mo, H. J., Mao, S., & White, S. D. M. 1998, *MNRAS*, 295, 319
- Nakamura, O., Aragón-Salamanca, A., Milvang-Jensen, B., et al. 2006, *MNRAS*, 366, 144
- Nesvadba, N. P. H., Lehnert, M. D., Eisenhauer, F., et al. 2006, *ApJ*, 650, 693
- Nesvadba, N. P. H., Lehnert, M. D., Genzel, R., et al. 2007, *ApJ*, 657, 725
- Nesvadba, N. P. H., Lehnert, M. D., Davies, R. I., Verma, A., & Eisenhauer, F. 2008, *A&A*, 479, 67
- Pizagno, J., Prada, F., Weinberg, D. H., et al. 2007, *AJ*, 134, 945
- Pozzetti, L., Bolzonella, M., Lamareille, F., et al. 2007, *A&A*, 474, 443
- Puech, M., Flores, H., Hammer, F., et al. 2008, *A&A*, 484, 173
- Reddy, N. A., Erb, D. K., Steidel, C. C., et al. 2005, *ApJ*, 633, 748
- Rudnick, G., Labbé, I., Förster Schreiber, N. M., et al. 2006, *ApJ*, 650, 624
- Saracco, P., Longhetti, M., Severgnini, P., et al. 2003, [arXiv:astro-ph/0312097]
- Shapiro, K. L., Genzel, R., Förster Schreiber, N. M., et al. 2008, *ApJ*, 682, 231
- Springel, V., Frenk, C. S., & White, S. D. M. 2006, *Nature*, 440, 1137
- Steidel, C. C., Adelberger, K. L., Shapley, A. E., et al. 2003, *ApJ*, 592, 728
- Stewart, K. R., Bullock, J. S., Wechsler, R. H., Maller, A. H., & Zentner, A. R. 2008, *ApJ*, 683, 597
- Swinbank, A. M., Bower, R. G., Smith, G. P., et al. 2007, *MNRAS*, 376, 479
- Swinbank, A. M., Webb, T. M., Richard, J., et al. 2009, *MNRAS*, 400, 1121
- Tacconi, L. J., Genzel, R., Neri, R., et al. 2010, *Nature*, 463, 781
- Tully, R. B., & Fisher, J. R. 1977, *A&A*, 54, 661
- van Dokkum, P. G., Quadri, R., Marchesini, D., et al. 2006, *ApJ*, 638, L59
- Vogt, N. P., Forbes, D. A., Phillips, A. C., et al. 1996, *ApJ*, 465, L15
- Wright, S. A., Larkin, J. E., Barczys, M., et al. 2007, *ApJ*, 658, 78
- Wright, S. A., Larkin, J. E., Law, D. R., et al. 2009, *ApJ*, 699, 421